Earth, Planets and Space

FULL PAPER

Open Access

Observing Earth's magnetic environment with the GRACE-FO mission

C. Stolle[1,2*], I. Michaelis[1], C. Xiong[1], M. Rother[1], Th. Usbeck[3], Y. Yamazaki[1], J. Rauberg[1] and K. Styp-Rekowski[1,4]

Abstract

The Gravity Recovery and Climate Experiment Follow-On (GRACE-FO) mission carries magnetometers that are dedicated to enhance the satellite's navigation. After appropriate calibration and characterisation of artificial magnetic disturbances, these observations are valuable assets to characterise the natural variability of Earth's magnetic field. We describe the data pre-processing, the calibration, and characterisation strategy against a high-precision magnetic field model applied to the GRACE-FO magnetic data. During times of geomagnetic quiet conditions, the mean residual to the magnetic model is around 1 nT with standard deviations below 10 nT. The mean difference to data of ESA's Swarm mission, which is dedicated to monitor the Earth's magnetic field, is mainly within ± 10 nT during conjunctions. The performance of GRACE-FO magnetic data is further discussed on selected scientific examples. During a magnetic storm event in August 2018, GRACE-FO reveals the local time dependence of the magnetospheric ring current signature, which is in good agreement with results from a network of ground magnetic observations. Also, derived field-aligned currents (FACs) are applied to monitor auroral FACs that compare well in amplitude and statistical behaviour for local time, hemisphere, and solar wind conditions to approved earlier findings from other missions including Swarm. On a case event, it is demonstrated that the dual-satellite constellation of GRACE-FO is most suitable to derive the persistence of auroral FACs with scale lengths of 180 km or longer. Due to a relatively larger noise level compared to dedicated magnetic missions, GRACE-FO is especially suitable for high-amplitude event studies. However, GRACE-FO is also sensitive to ionospheric signatures even below the noise level within statistical approaches. The combination with data of dedicated magnetic field missions and other missions carrying non-dedicated magnetometers greatly enhances related scientific perspectives.

Keywords: Earth's magnetic field, Geomagnetism, Ionospheric currents, Magnetospheric ring current, Satellite-based magnetometers, Platform magnetometers, GRACE-FO

Introduction

Low Earth orbiting (LEO) satellite missions dedicated to accurately measure the geomagnetic field have revolutionised the capability of monitoring Earth's magnetic field. The first of these missions was MAGSAT, followed by Ørsted, SAC-C, CHAMP, and recently Swarm. These missions enabled studies of the recent evolution of the core field (e.g., Hulot et al. 2002; Livermore et al. 2017), global lithospheric field mapping on scales between 200 and 3000 km (e.g., Maus et al. 2007; Olsen et al. 2017), and the altitude-dependent description of the Earth's mantle conductivity (e.g., Grayver et al. 2016) to what concerns geomagnetic sources located at Earth's interior. Concerning the exploration of the geospace environment, geomagnetic LEO missions have especially contributed by first possible observations of currents flowing in the ionosphere that are only detectable by in situ measurements. These include polar cusp, auroral, and inter-hemispheric field-aligned currents (e.g., Olsen 1997; Lühr et al. 2017; McGranaghan et al. 2017), vertical currents at the magnetic equator (e.g., Park et al. 2010), F region gravity-driven and plasma-pressure-driven currents (e.g., Alken 2016; Laundal et al. 2019), or diamagnetic

*Correspondence: cstolle@gfz-potsdam.de
[1] Helmholtz Centre Potsdam, GFZ German Research Centre for Geosciences, Telegrafenberg, 14473 Potsdam, Germany
Full list of author information is available at the end of the article

and field-aligned currents connected to irregularities at equatorial or mid-latitudes (e.g., Rodríguez-Zuluaga and Stolle 2019; Park et al. 2010; Stolle et al. 2006). A comprehensive review on achievements by high-precision geomagnetic data from space and their applications is given, e.g., by Olsen and Stolle (2012).

In addition, high-amplitude signatures of electric currents in the ionosphere and magnetosphere have been detected by observations from magnetometers at LEO altitude that do not meet the accuracy of the above-mentioned dedicated geomagnetic missions. These are either non-high-precision magnetic observations, e.g., the mission did not measure the magnitude of the total field together with the variations of the magnetic components, or it did not carry an optical bench on the magnetometer boom (e.g., CSES, C/NOFS, DMSP, and e-POP, in the following examples). Another category are so-called platform magnetometers which are mounted at the satellite body and are primarily used for attitude determination (e.g., AMPERE, CryoSat-2, GRACE, and GRACE-FO, in the following examples). With its constellation of 66 satellites, maps of auroral field-aligned currents derived from magnetometer data of the AMPERE project have had large impact on the investigations of the polar ionosphere (e.g., Anderson et al. 2000; Korth et al. 2010; Carter et al. 2016). The magnetometers on the DMSP satellites were used, e.g., to derive Poynting Flux at auroral latitudes (Knipp et al. 2011) or to describe the relation of the location between auroral FACs and particle energy flux (Xiong et al. 2020). CASSIOPE e-POP data were used to derive fine structures of auroral arcs (Miles et al. 2018), and observations from the low-inclination satellite C/NOFS added in describing the local time dependence of the geomagnetic signal due to the magnetospheric ring currents during geomagnetic active times (Le et al. 2011). However, recently, Park et al. (2020) demonstrated that statistical analyses of multiple years of field-aligned current data derived from magnetometer observations of the CryoSat-2 and GRACE-FO missions successfully revealed mid-latitude inter-hemispheric currents. This finding is especially interesting, because it proves the capability of data from non-dedicated magnetometers to be sensitive to small amplitude currents, as well.

Also core field structures have successfully been derived from these types of data. Magnetometer data from DMSP were applied for geomagnetic field modelling in a spherical harmonic expansion up to degree 15 (Alken et al. 2014). A special consideration of data from DMSP and ESA's CryoSat-2 was taken to enhance the data availability between the re-entry of CHAMP in 2010 and the launch of the Swarm mission in 2013 (e.g., Alken et al. 2020a; Finlay et al. 2020). Data from the recently launched CSES mission of the China Earthquake Administration have provided a candidate model for the International Geomagnetic Reference Field (IGRF-13) (Alken et al. 2020b; Yang et al. 2020).

Different characterisation and calibration strategies for non-high-precision magnetometers in space have been applied, e.g., on data of the AMPERE, DMSP, CryoSat-2, or GRACE missions [e.g., Anderson et al. 2000; Alken et al. 2014, 2020a; Olsen et al. 2020, Olsen (submitted to Earth, Planets, and Space)]. This article introduces a calibrated magnetometer data set for the Gravity Recovery and Climate Experiment Follow-On (GRACE-FO) mission.

The GRACE-FO mission is operated under a partnership between NASA and the German Research Centre for Geosciences (GFZ). The primary objective of GRACE-FO (Landerer et al. 2020) is to obtain precise global and high-resolution models for both the static and the time variable components of the Earth's gravity field. It is a successor to the original GRACE mission (Tapley et al. 2004), which orbited Earth from March 2002 until October 2017.

GRACE-FO was successfully launched on 22 May 2018. It is a constellation mission and the two identical satellites, named GF1 and GF2 in the following, fly at the same orbit but with GF1 leading GF2 by a distance of approximately 220 km. They fly on a near-circular polar orbit with an inclination of 89° and at an altitude of 490 (±10) km. A sketch of its formation is illustrated in Fig. 1 and a summary on 'quick facts' on satellite orbits and bodies is available at https://gracefo.jpl.nasa.gov/overlay-quick-facts/.

As part of their attitude orbit control system (AOCS), the GRACE-FO satellites carry magnetometers and this article introduces a calibrated magnetometer data set of GF1 and GF2. We first describe the original data and the data pre-processing which we applied, followed by describing the applied calibration and characterisation techniques. The final data set is assessed, and it is compared against Swarm observations during conjunction events between the two missions. Finally, we discuss the performance of the prepared data set for scientific applications on selected example areas. The processed magnetometer data published by this article are available at ftp://isdcftp.gfz-potsdam.de/grace-fo/MAGNETIC_FIELD/, currently for 29 months between June 01, 2018 and October 31, 2020. The data set is extended with continuing mission operation. The data published with this article are version *0201*.

Data sets and data pre-processing

As part of the attitude orbit control system (AOCS), each GRACE-FO satellite carries two fluxgate magnetometers (FGM), an active one, FGM A, and a redundant

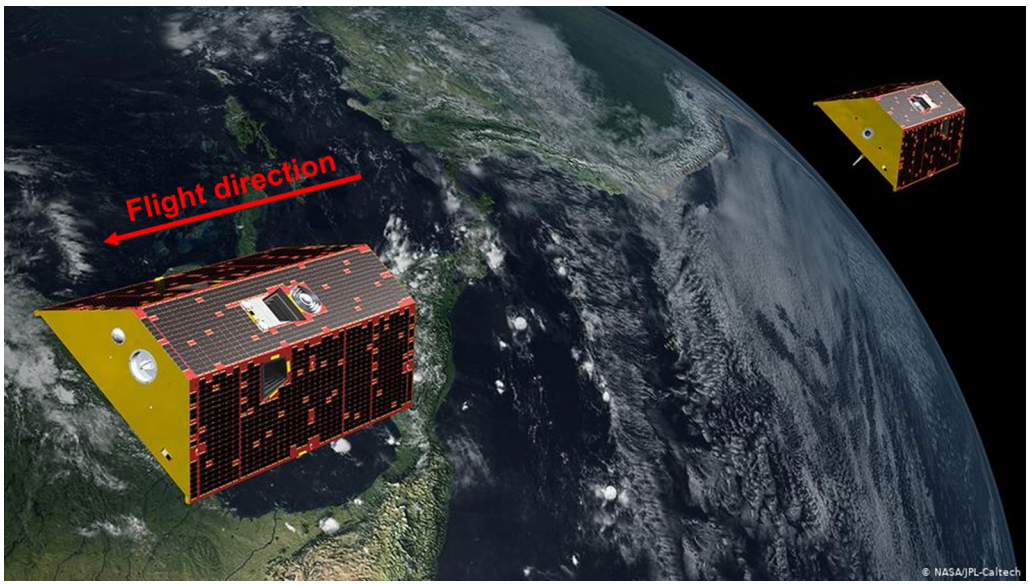

Fig. 1 Schematic view of the GRACE-FO constellation mission (credits: NASA/JPL-Caltech)

one, FGM B. So far, the redundant magnetometers were not switched on for GF1 and only on few days for GF2 in February 2019. The left panel in Fig. 2 shows the location of the magnetometers on board the satellite. The magnetometers are manufactured by Billingsley Aerospace & Defence and are of type TFM100SH (Billingsley 2020). The measurement range is $\pm 65{,}000$ nT and the root-mean-square noise level is ~ 60 pT/$\sqrt{\text{Hz}}$. The data are sampled at 1 Hz as spot values with no on-board filtering from higher frequency data.

Magnetometer calibration further relies on attitude data derived from the three star cameras (STR) that are mounted at the top and at each side of the satellite (indicated by squared black open cylinders in Fig. 1).

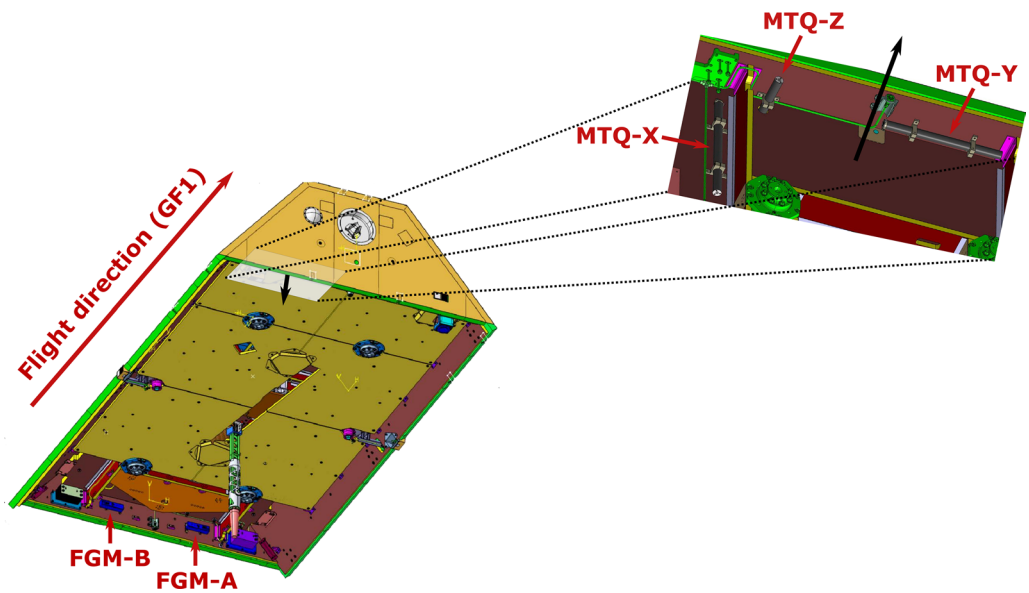

Fig. 2 (Left) location of FGMs at the satellite body. Flight direction (red arrow) is indicated for GF1. GF2 has opposite flight direction. (Right) location of the magnetorquers at the bottom side of the satellite. Black arrows in both panels indicate the normal vector to the satellite bottom. In the left panel, the magnetorquers are hidden by the front plate (credits: AIRBUS)

Among others, magnetic perturbation is often expected from magnetorquers (MTQ) that are mounted to steer pitch, yaw, and roll, respectively. At the GRACE-FO satellites, they are located at the opposite side of the satellite body than the magnetometers do and their location is indicated in the right panel of Fig. 2. GRACE-FO magnetometer, magnetorquer currents, and attitude data are part of the mission's L1b data sets and are available at ftp://isdcftp.gfz-potsdam.de/grace-fo/. To characterise the magnetic data, we also used information on magnetometer temperature, battery currents, and solar array currents. These data can be accessed on request from the Information System and Data Centre (ISDC) at GFZ Potsdam. An overview of used input data is given in Table 1. GRACE-FO L1b data are provided in zip files that contain ASCII files for each L1b product listed in Table 1. Each file consists of a header and a data part, and time values are always handled as GPS time. Most of L1b data are provided in 1 Hz resolution. However, magnetorquer currents comes in 2 Hz. The sampling rate of the magnetometers is 1 Hz, but they have been simulated in the L1b files being 2 Hz by doubling each 1 Hz sample to technically be in concert with MTQ sampling rates. Therefore, we ignore each second record from MAG1B. Additionally, we found that the magnetorquer currents saturate at ± 110 mA. Due to this limitation, we de-selected all values that coincide with the saturated values to later avoid possible misinterpretation during characterisation.

Since data time stamps are not all given on the full second, they are interpolated to a common time grid. We use the time stamps of the star camera data as the reference for the grid. All other products have been interpolated to these reference time stamps using linear interpolation. At these times and respective satellite locations, we further generated predictions of the core, the crustal, and the large-scale magnetospheric field by the CHAOS-7 model (Finlay et al. 2019, 2020). The modelled values will later be the reference during calibrations of GRACE-FO magnetic data. We also generated quasi-dipole latitude (QDLAT) and magnetic local time (MLT) (Richmond 1995; Emmert et al. 2010) for each GRACE-FO record, that will help in data selection for calibration and finally during the assessment of the calibration results. We are later interested to assess magnetic data in the Earth-fixed North-East-Centre (NEC) reference frame; also, CHAOS-7 predicts field data in NEC, further used as $\mathbf{B}_{\mathbf{model,NEC}}$. However, since the estimated calibration parameters are instrument intrinsic and calibration is performed in this instrument frame of the magnetometers (called FGM frame in the following), appropriate rotations need to be applied. Earth's nutation and precession rotation matrix needed to rotate between the International Terrestrial Reference Frame (ITRF) and the International Celestial Reference Frame (ICRF) are

Table 1 Input data used for calibration and characterisation, including product name (if applicable), variable name, unit, and temporal resolution

	Description	Product	Variable	Unit	Resolution
E	Magnetic field	MAG1B	MfvX_RAW	nT	1 s
			MfvY_RAW		
			MfvZ_RAW		
$\mathbf{A_{MTQ}}$	Magnetorquer currents	MAG1B	torque1A, torque1B	mA	0.5 s
	Positive X, negative X		torque2A, torque2B		
	Positive Y, negative Y		torque3A, torque3B		
	Positive Z, negative Z				
POS	Satellite position in ITRF	GNV1B	xpos, ypos, zpos	m	1 s
STR	Rotation from ICRF to FGM in quaternion representation	SCA1B	quaticoeff		1 s
			quatjcoeff		
			quatkcoeff		
			quatangle		
$\mathbf{T_{FGM}}$	Magnetometer temperature		THT10060	°C	32 s
$\mathbf{A_{BAT}}$	Battery current		PHT10016	A	1 s
			PHT10017		
			PHT10018		
$\mathbf{A_{SA}}$	Solar array current		PHT10030	A	1 s
			PHT10036		
			PHT10041		

obtained by applying (IAU SOFA Board 2019, SOFAlibaryfunctioniauC2t06a), where Earth rotation parameters are derived from the International Earth Rotation and Reference Systems service (IERS 2020). The rotation matrix between the ITRF and the ICRF frame, $\underline{R_{\mathrm{ITRF2NEC}}}$, is then determined for respective time and Earth rotation parameters. The rotation matrix between ITRF and NEC depends on geocentric location (latitude and longitude). The equation is based on Seeber (2003, p. 23) for a North-East-Zenith frame but changing the sign of the z-direction (3rd row) to get a right-handed North-East-Center frame (NEC). The rotation matrix is described as:

$$\underline{R_{\mathrm{ITRF2NEC}}} = \begin{vmatrix} -\sin(\Phi)\cdot\cos(\Lambda) & -\sin(\Phi)\cdot\sin(\Lambda) & \cos(\Phi) \\ -\sin(\Lambda) & \cos(\Lambda) & 0 \\ -\cos(\Phi)\cdot\cos(\Lambda) & -\cos(\Phi)\cdot\sin(\Lambda) & -\sin(\Phi) \end{vmatrix} \tag{1}$$

with latitude Φ and longitude Λ.

In the case of the GRACE-FO L1b data, both magnetometer and star camera data are provided in the same frame, the Science Reference Frame (SRF) (Note that this might not be the case for other missions). SRF is a spacecraft frame and it has its origin at the center of mass of the accelerometer proof mass, the x-axis is aligned with the roll axis, the y-axis is aligned with the pitch axis, and the z-axis is aligned with the yaw axis of the satellite. Remaining misalignment between the orientation of the FGM instrument and the SRF frame is later reflected within the Euler angles during calibration.

The satellite attitude data provided by the star cameras are given in a combined product for all 3 star cameras and are in quaternion representation, which led us to perform all rotations by quaternion notation. The rotation from the SRF to the ICRF frame is directly given by the star camera data. Since both the FGM and star camera data are given in SRF, their rotation to ICRF is identical to q_{FGM2ICRF}. Conversion of the direction cosine matrices, $\underline{R_{\mathrm{ITRF2NEC}}}$ and $\underline{R_{\mathrm{NEC2ITRF}}}$, to quaternion representations is realised by a function, F_λ, following Wertz (1978, p. 415) and $q_{\mathrm{NEC2ITRF}} = F_\lambda(\underline{R_{\mathrm{ITRF2NEC}}}^{-1})$ and $q_{\mathrm{ITRF2ICRF}} = F_\lambda(\underline{R_{\mathrm{ITRF2NEC}}})$. In summary, the complete rotation from the NEC to the FGM frame is given as:

$$\mathbf{q_{NEC2FGM}} = \mathbf{q_{NEC2ITRF}} \cdot \mathbf{q_{ITRF2ICRF}} \cdot \mathbf{q_{FGM2ICRF}^{-1}} \tag{2}$$

$$\mathbf{B_{NEC}} \xrightarrow{\mathbf{q_{NEC2ITRF}}} \mathbf{B_{ITRF}} \xrightarrow{\mathbf{q_{ITRF2ICRF}}} \mathbf{B_{ICRF}} \xrightarrow{\mathbf{q_{FGM2ICRF}^{-1}}} \mathbf{B_{FGM}}. \tag{3}$$

CHAOS-7 predictions are finally rotated from NEC to the FGM frame applying the rotation quaternion in Eq. 2 following Wertz (1978, p. 759):

$$\mathbf{B_{model,FGM}} = \mathbf{q_{NEC2FGM}^{-1}} \cdot \mathbf{B_{model,NEC}} \cdot \mathbf{q_{NEC2FGM}}. \tag{4}$$

Calibration and characterisation described in the next section are performed in the instrument FGM frame. For later interpretation of the data in the geophysical NEC frame, the calibrated data are rotated back applying the inverse of Eq. 3.

Calibration and characterisation

The magnetometer data of GRACE-FO are pre-calibrated on board to satisfy attitude and orbiting control via AOCS. These magnetometer data are provided in the L1b data. However, the characterisation of the data for artificial disturbances and further calibration are needed for application in scientific studies. The applied calibration and characterisation approach is similar to that applied by Olsen et al. (2020), but a somewhat higher time variability was allowed for the estimated parameters applied. Calibration and characterisation have been performed on subsets of monthly data and for a subsample within each month satisfying $|\mathrm{QDLAT}| < 50°$, $\mathrm{Kp} \leq 2$, $|\mathrm{Dst}| \leq 30\,\mathrm{nT}$ and B_Flag = 0. The flag B_Flag differs from zero if one of the magnetorquers is saturated. Selecting monthly sets is a compromise between high fluctuations of calibration and characterisation parameters that would occur for daily processing, but still capturing possible long-term trends of the parameters.

An ordinary least-squares linear regression was applied to these subsets:

$$S = |(\mathbf{B_{cal}}(\mathbf{m_{cal}}, \mathbf{E}) + \mathbf{B_{char}}(\mathbf{m_{char}}, \mathbf{d_{HK}})) - \mathbf{B_{model,FGM}}|^2, \tag{5}$$

where $\mathbf{B_{cal}}$ is the calibrated magnetic field vector after calibration parameters $\mathbf{m_{cal}} = (\mathbf{b}, \mathbf{s}, \mathbf{u}, \mathbf{e}, \underline{\xi}, \underline{\nu})$ have been applied on the raw magnetic field vector $\mathbf{E}$ (see also Eq. 9). $\mathbf{B_{char}}$ is the estimated vector describing the artificial magnetic field from the satellite derived by the application of the characterisation parameters $\mathbf{m_{char}} = (\underline{M}, \underline{\mathrm{bat}}, \underline{\mathrm{sa}}, \underline{\mathrm{bt}}, \underline{\mathrm{st}})$ on the so-called housekeeping data $\mathbf{d_{HK}} = (\mathbf{A_{MTQ}}, \mathbf{A_{BAT}}, \mathbf{A_{SA}}, \mathbf{T_{FGM}}, \mathbf{E_{st}})$ (see also Eq. 13). $\mathbf{B_{model,FGM}}$ includes the CHAOS-7 magnetic field estimations for both the core, crustal, and large-scale magnetospheric field rotated into the instrument FGM frame as described in Eq. 4. The parameters $\mathbf{m_{cal}}$ and $\mathbf{m_{char}}$ are optimized to reduce the defined squared error S.

Additionally, the calibration has been applied with different time-shifts of the magnetometer data set to account for possible time stamp errors. Within an interval of ± 2 s, the data set was shifted in steps of 0.1 s and again in steps of 0.01 s around the most probable target. This investigation was applied on the most quiet data set which was in January 2019. Best calibration results (minimum of the absolute values of residual to CHAOS-7) have been determined for GF1 with 0.95 s for FGM

data and for GF2 with 0.73 s for FGM data. For GF2, the residual was even smaller after time-shifts have also been applied to housekeeping data, −10 s for solar array currents, 2 s for battery currents, and 0.3 s for magnetorquer currents. For GF1, additional time-shifts on housekeeping data did not reduce the residual and zero time-shift was kept for housekeeping data. These time-shifts have been applied to the magnetometer and/or housekeeping data, respectively, before the final calibration and characterisation was performed. Applying these time-shifts gave evenly large or reduced residuals for each months in the calibrated period.

Parameters for calibration

The raw magnetic field vector provided by the L1b data is represented in the three directional components within the instrument FGM frame as $\mathbf{E} = (E_1, E_2, E_3)^{\mathrm{T}}$ (see Table 1 for corresponding field names) given in units of nT. The calibration approach estimates nine intrinsic and three external parameters. Six of the intrinsic parameters are included in an offset vector $\mathbf{b} = (b_1, b_2, b_3)^{\mathrm{T}}$ and a scale vector $\mathbf{s} = (s_1, s_2, s_3)^{\mathrm{T}}$. Ideally, the coils of the FGMs are perfectly perpendicular to each other. To account for an inexactness, a misalignment angle vector $\mathbf{u} = (u_1, u_2, u_3)^{\mathrm{T}}$ includes the other three intrinsic parameters. The orientation of the instrument with respect to the SRF is given in the specification of the satellite, or in the case of the AOCS magnetometer of GRACE-FO, these frames are identical in the L1b data. In practice, also this orientation is not perfectly constant. Misalignment of it is given in a vector of Euler (1–2–3) angle representation $\mathbf{e} = (e_1, e_2, e_3)^{\mathrm{T}}$, following Wertz (1978, p. 764), or in a direction cosine rotation matrix, $\underline{R_A}$, which includes the three external parameters. Euler (1–2–3) represents three rotations about the first, second, and third axis, in this order. The parameters are used to describe:

$$\mathbf{B_{cal}} = \underline{R_A}\underline{P}^{-1}\underline{S}^{-1}(\mathbf{E} - \mathbf{b}) = \underline{A}(\mathbf{E} - \mathbf{b}) = \underline{A}\mathbf{E} - \mathbf{b_A}, \tag{6}$$

where $\underline{R_A}$ is the direction cosine matrix representation of the Euler (1–2–3) angles $\mathbf{e}$, $\underline{P}^{-1}$ is the misalignment angle lower triangular matrix with:

$$\underline{P}^{-1} = \begin{vmatrix} 1 & 0 & 0 \\ \frac{\sin(u_1)}{\cos(u_1)} & \frac{1}{\cos(u_1)} & 0 \\ -\frac{\sin(u_1)\sin(u_3)+\cos(u_1)\sin(u_2)}{w\cos(u_1)} & -\frac{\sin(u_3)}{w\cos(u_1)} & 1/w \end{vmatrix}$$
$$\text{with: } w = \sqrt{1 - \sin^2(u_2) - \sin^2(u_3)}, \tag{7}$$

and $\underline{S}^{-1}$ is the diagonal matrix including the inverse of the scale factor:

$$\underline{S}^{-1} = \begin{vmatrix} 1/s_1 & 0 & 0 \\ 0 & 1/s_2 & 0 \\ 0 & 0 & 1/s_3 \end{vmatrix}. \tag{8}$$

Equation 6 is valid, if, in first order, fluxgate magnetometers are treated as linear instruments. If the condition of linearity is not given (Brauer et al. 1997), a linearised equation is applied by extending Eq. 6 for non-linear effects of second ($\underline{\xi}$) and third ($\underline{\nu}$) order parameters applied on second- ($\mathbf{E}_\xi$) and third-order ($\mathbf{E}_\nu$) data:

$$\mathbf{B_{cal}} = \underline{A}\mathbf{E} - \mathbf{b_A} + \underline{\xi}\mathbf{E}_\xi + \underline{\nu}\mathbf{E}_\nu, \tag{9}$$

with non-linearity parameters of second order:

$$\underline{\xi} = \begin{vmatrix} \xi^1_{11} & \xi^1_{22} & \xi^1_{33} & \xi^1_{12} & \xi^1_{13} & \xi^1_{23} \\ \xi^2_{11} & \xi^2_{22} & \xi^2_{33} & \xi^2_{12} & \xi^2_{13} & \xi^2_{23} \\ \xi^3_{11} & \xi^3_{22} & \xi^3_{33} & \xi^3_{12} & \xi^3_{13} & \xi^3_{23} \end{vmatrix}, \tag{10}$$

non-linearity parameters of third order:

$$\underline{\nu} = \begin{vmatrix} \nu^1_{111} & \nu^1_{222} & \nu^1_{333} & \nu^1_{112} & \nu^1_{113} & \nu^1_{223} & \nu^1_{122} & \nu^1_{133} & \nu^1_{233} & \nu^1_{123} \\ \nu^2_{111} & \nu^2_{222} & \nu^2_{333} & \nu^2_{112} & \nu^2_{113} & \nu^2_{223} & \nu^2_{122} & \nu^2_{133} & \nu^2_{233} & \nu^2_{123} \\ \nu^3_{111} & \nu^3_{222} & \nu^3_{333} & \nu^3_{112} & \nu^3_{113} & \nu^3_{223} & \nu^3_{122} & \nu^3_{133} & \nu^3_{233} & \nu^3_{123} \end{vmatrix}, \tag{11}$$

and modulated data vectors of second and third order:

$$\begin{aligned} \mathbf{E}_\xi &= (E_1^2,\, E_2^2,\, E_3^2,\, E_1E_2,\, E_1E_3,\, E_2E_3)^{\mathrm{T}} \\ \mathbf{E}_\nu &= (E_1^3,\, E_2^3,\, E_3^3,\, E_1^2E_2,\, E_1^2E_3, \\ &\quad E_2^2E_3,\, E_1E_2^2,\, E_1E_3^2,\, E_2E_3^2,\, E_1E_2E_3)^{\mathrm{T}}. \end{aligned} \tag{12}$$

Parameters for characterisation

Characterisation consists of the identification and, if possible, correction of artificial magnetic perturbations contained in the raw magnetic data. We identified the magnetorquer currents, $\mathbf{A_{MTQ}}$, the magnetometer temperature, $\mathbf{T_{FGM}}$, the battery currents, $\mathbf{A_{BAT}}$, and the solar array panel currents, $\mathbf{A_{SA}}$, to affect the GRACE-FO magnetometer data. We also consider an effect from the correlation between the magnetometer temperature and magnetic field residuals, $\mathbf{E_{st}} = \mathbf{E} \cdot (\mathbf{T_{FGM}} - T_0)$, where T_0 is the monthly median of $\mathbf{T_{FGM}}$.

The characterisation equation is a combination of all identified disturbances:

$$\begin{aligned} \mathbf{B_{char}} = &\underline{M} \cdot \mathbf{A_{MTQ}} + \underline{\mathrm{bat}} \cdot \mathbf{A_{BAT}} + \underline{\mathrm{sa}} \cdot \mathbf{A_{SA}} \\ &+ \underline{\mathrm{bt}} \cdot (\mathbf{T_{FGM}} - T_0) + \underline{\mathrm{st}} \cdot \mathbf{E_{st}}. \end{aligned} \tag{13}$$

For both Eqs. 9 and 13, input variables and parameters to be estimated are summarised in Tables 1 and 2, respectively. Both the estimated parameters and the calibrated magnetic observation products are provided on the ISDC ftp site.

Table 2 Estimated calibration and characterisation parameters including units and dimensionality

Parameter	Description	Unit	Dimension
s	Scale factors	$\frac{nT}{nT}$	3
b	Offsets	nT	3
u	Misalignment angles	rad	3
e	Euler (123) angles	rad	3
$\underline{\xi}$	2nd order non-linearity	$\frac{nT}{nT^2}$	3×6
$\underline{\nu}$	3rd order non-linearity	$\frac{nT}{nT^3}$	3×10
$\underline{bt}$	Temperature dependency of offsets b	$\frac{nT}{°C}$	3×3
$\underline{st}$	Temperature dependency of scale factors s	$\frac{nT}{nT\,°C}$	3×3
$\underline{bat}$	Battery current scale factor	$\frac{nT}{mA}$	3×3
$\underline{sa}$	Solar array current scale factor	$\frac{nT}{mA}$	3×3
$\underline{M}$	Magnetorquer current scale factor	$\frac{nT}{mA}$	3×3

Results and discussion

This section discusses the final GRACE-FO data set and its application. We assess the residuals to CHAOS-7 predictions of all vector components and perform an independent validation by comparison to high-precision observations from the simultaneous Swarm mission, e.g., during orbit conjunctions or close flybys. By discussing selected scientific applications on auroral field-aligned currents and signatures of the magnetospheric ring current, this section aims at further outlining opportunities and limitations of the GRACE-FO data set.

Assessment of final data set

Table 3 provides the mean and the standard deviations of the residuals of the final magnetic field vector of GF1 and GF2 to CHAOS-7 predictions for $|\mathrm{QDLAT}| < 50°$, $\mathrm{Kp} \leq 2$, and $|\mathrm{Dst}| \leq 30\,\mathrm{nT}$. Averaged over the entire period of GRACE-FO, the mean is zero, which is not surprising, since the data have been calibrated against CHAOS-7. The standard deviation is few nanotesla and is in general a bit higher for GF2 than for GF1. For a single day, the standard deviations do not differ significantly from the one of the entire period, but the mean is slightly biased. For comparison, the lower rows in Table 3 provide the values for the raw magnetic data provided in L1b. Both mean and standard deviation have dramatically been reduced after calibration and characterisation. The amplitudes in standard deviation of few nanoteslas are similar to those of the root mean scatter of the CryoSat-2 residuals discussed in Olsen et al. (2020), which varied between 4 and 15 nT depending on local time and geomagnetic activity. This agreement is especially remarkable, because CryoSat-2 carries three identical magnetometers, and Olsen et al. (2020) compares the mean of their calibrated times series, which further reduces the effect of the intrinsic noise from the single instruments.

To estimate the impact of the different parameters on the final results, Eq. 5 was applied but omitting single parameters in Table 2 in each application. The standard deviation of the residuals to CHAOS-7 for each of these applications is given in Table 4 for both GF1 and GF2. The minimum and maximum values of the residuals of each respective result are also provided. Largest standard deviation is observed when solar array and battery currents are not considered in the characterisation. Large spikes or jumps can be corrected with knowledge of the magnetorquer currents. For GF2, battery currents and solar arrays have larger impact than for GF1. Also, on GF2, the temperature dependence of the scale factor is an important parameter.

Table 3 Mean and standard deviation of residuals to CHAOS-7 for GF1 and GF2 for geomagnetic quiet times and for a single quiet day, 30 January 2019

Parameter	Whole period						Single day					
	Mean (nT)			Std (nT)			Mean (nT)			Std (nT)		
	x	*y*	*z*	*x*	*y*	*z*	*x*	*y*	*z*	*x*	*y*	*z*
GF1												
ΔB_{NEC}	0.0	0.0	0.0	7.8	7.9	9.5	−0.2	−0.6	−0.6	4.3	5.2	2.9
ΔB_{RAW}	−323.1	−551.5	78.3	95.7	323.1	131.8	−302.4	−561.5	85.1	97.3	321.5	130.5
GF2												
ΔB_{NEC}	0.0	0.0	0.0	7.1	8.4	7.7	0.4	−2.0	1.2	3.9	8.0	3.6
ΔB_{RAW}	1357.3	351.7	−145.9	285.6	204.5	116.5	1331.5	380.1	−173.1	295.3	206.8	116.6

B_{NEC} represents residuals for calibrated data and B_{RAW} for data before calibration

Table 4 Magnetic impact of calibration and characterisation, respectively, for each parameter given in Eq. 13 and the non-linear parameters in Eq. 9

Parameter	Std (nT)			Min (nT)			Max (nT)		
	x	*y*	*z*	*x*	*y*	*z*	*x*	*y*	*z*
GF1									
$\Delta\mathbf{B}_{\xi}$	5.2	6.9	3.8	−28.1	−67.9	−38.6	21.5	25.8	20.3
ΔB_{ν}	7.6	9.6	5.4	−46.0	−45.8	−37.5	47.2	75.1	66.3
ΔB_{MTQ}	8.6	6.2	6.8	−230.5	−209.5	−578.7	242.5	206.4	263.0
ΔB_{BAT}	17.0	29.5	18.4	−309.4	−343.1	−354.2	196.5	536.8	225.6
ΔB_{SA}	66.3	112.0	74.4	−503.4	−174.3	−554.2	106.6	863.8	262.1
ΔB_{BT}	1.9	3.2	1.6	−16.2	−17.8	−18.2	16.9	28.6	10.4
ΔB_{ST}	5.5	2.2	8.1	−175.8	−16.0	−204.1	167.3	20.0	217.5
$\Delta B_{\mathrm{cal,NEC}}$	7.8	7.9	9.5	−220.6	−112.2	−287.7	217.9	161.8	329.0
GF2									
ΔB_{ξ}	5.1	7.8	4.2	−17.7	−28.6	−19.6	28.7	28.7	34.1
ΔB_{ν}	10.1	9.1	5.6	−100.7	−49.1	−48.5	74.0	43.9	35.9
ΔB_{MTQ}	10.2	6.6	6.9	−222.8	−235.3	−178.4	226.9	190.7	258.2
ΔB_{BAT}	21.1	21.4	18.6	−131.1	−87.8	−100.6	66.8	87.5	136.9
ΔB_{SA}	19.2	35.1	29.0	−60.0	−184.2	−230.4	85.0	166.1	117.1
ΔB_{BT}	4.1	6.9	4.5	−44.5	−26.4	−11.9	30.1	114.5	81.6
ΔB_{ST}	9.3	3.2	14.6	−273.3	−26.0	−390.6	244.0	29.2	317.8
$\Delta B_{\mathrm{cal,NEC}}$	7.1	8.4	7.7	−6364.5	−121.8	−277.8	180.9	1013.9	7208.9

Results are given in the FGM (SRF) reference frame for GF1 and GF2

Figure 3 provides residuals between the processed data and CHAOS-7 predictions for January 2019, e.g., their mean of all residuals within each bin of a grid with bin size of 5° geocentric latitude and 5° geocentric longitude. The four columns are for the B_{N}, B_{E}, and B_{C} component of the NEC frame, respectively, and for the total field F. The first row displays residuals to the core, the crustal and the large-scale magnetospheric field predictions of CHAOS-7 for GF1, and the second row shows the same for GF2. The grey lines indicate the 0° and ±70° magnetic latitude (QDLAT). The third row shows the difference between GF1 and GF2 residuals. The last row gives geomagnetic and solar indices and magnetic local time of the data set of this month. Hence, the mission flew in a 07/19 MLT orbit and the month was geomagnetically very quiet. In both GF1 and GF2, largest deviations occur at auroral regions which result from the auroral electrojet and field-aligned currents. Since the data are collected at 07/19 MLT, no significant low- and mid-latitude ionospheric disturbances are expected, neither significant effects from magnetospheric currents during the quiet times. However, some systematic deviations occur, such as above the northern Atlantic in the ΔB_{E} and ΔB_{C} components of GF1 and the ribbon at low latitudes in ΔB_{C} of GF2. These could not be accounted for through correlation with any known satellite characteristic. However, residuals of 10 nT or less can be seen as an acceptable result for data from a non-dedicated magnetometer where magnetic cleanliness of the satellite has not explicitly been taken care of. The differences between the GF1 and GF2 residuals show similar amplitudes in mid and low latitudes, which indicates that artificial disturbances from the satellite are not identical between the two spacecraft. It is interesting to note that the statistics for calibrated CryoSat-2 magnetic data provided by Olsen et al. (2020) (not shown) reveal a similar behaviour. CryoSat-2 satellite carries three active magnetometers from the same type of Billingsley (Billingsley 2020) as does GRACE-FO, and, e.g., only B_{C} from one magnetometer (magnetometer 2) show a disturbance at the magnetic equator with similar amplitude than for B_{C} of GF2, but this effect is reduced or absent for the other two data sets of B_{C} of CryoSat-2. In contrast, high amplitudes due to auroral electric currents are largely reduced in the third row of Fig. 3, but did not vanish as could be expected from a natural signal. This fact hints to small-scale structures in the magnetic field at high latitudes that have shorter wavelengths than 20 s (Gjerloev et al. 2011), being the mean separation time between GF1 and GF2. These observations need detailed investigations, e.g., sorted for MLT or geomagnetic activity, to allow discrimination between natural and satellite intrinsic variability, which is currently beyond the scope of this paper. A first analysis, however, revealed that the positive differences

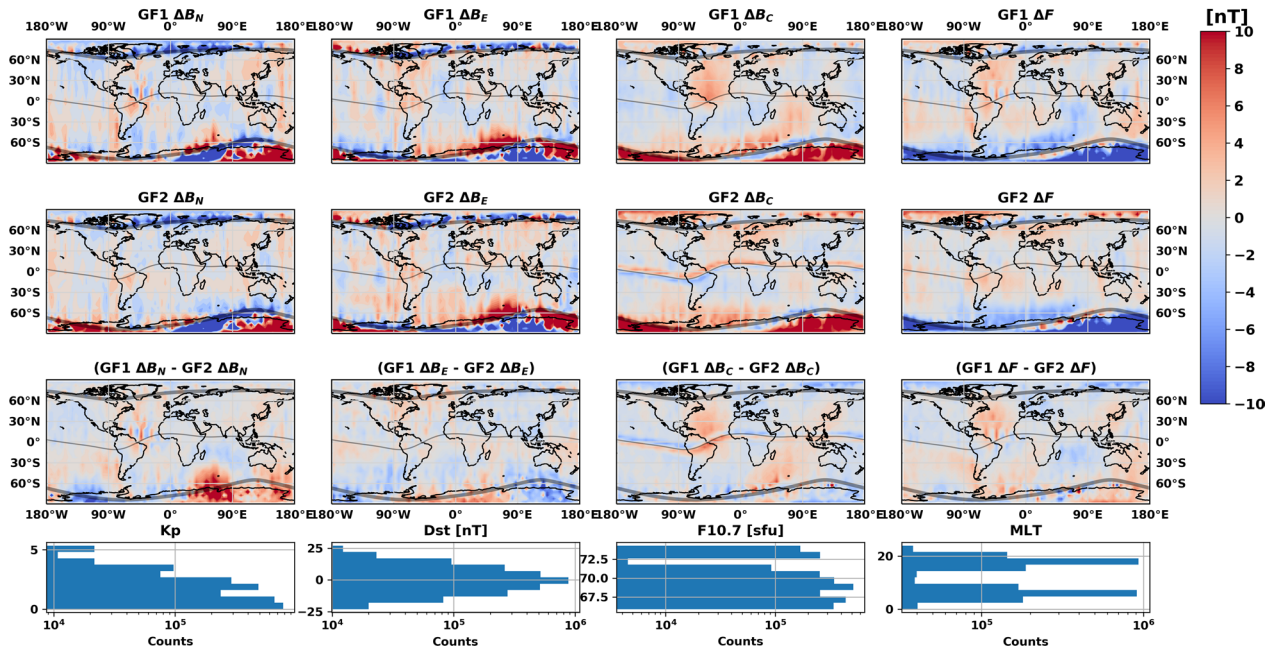

Fig. 3 Magnetic residuals to CHAOS-7 (core, crustal, and large-scale magnetospheric field) in the three NEC (left) components and the field magnitude, F, (right) for GF1 and GF2, respectively. The panels in the third row show the difference between GF1 and GF2 residuals. The fourth panel shows the distribution of geomagnetic and solar activity indices and magnetic local time

at around 30° E at the daylight Southern polar region accumulates around magnetic noon, which is the typical region of the polar cusp and known for small-scale structures. As the reader shall note, Fig. 3 represents one of the geomagnetic quietest months of the processed period of GRACE-FO data. The pattern changes from month to month and mean residuals up to 15 nT also at mid and low latitudes occur at other months.

Figure 4 provides orbit-wise residual vectors in the NEC frame for a period in September 2019 for ascending (∼ 12 MLT) and descending (∼ 00 MLT) orbits around noon and midnight, respectively. Top panel red lines show GF1 results and bottom panel blue lines GF2 results. Black lines provide mean values at each QDLAT. The geomagnetic activity was low with Kp ≤ 4 (median Kp = 1.3) and Dst > -30 nT (mean Dst $= -5.5$ nT). The significant variability of the single orbits indicates the day-to-day variability of ionospheric currents, and the statistical mean hints to typical ionospheric features. As expected, largest deviations occur at auroral latitudes. The negative excursion of B_N and the flip of sign towards negative towards North in B_C reflect signatures of the eastward equatorial electrojet. The amplitudes in both components of about 10 nT are consistent with signatures detected earlier in CHAMP (Lühr and Maus 2006). The flip of sign towards positive towards north in B_E with a few nanotesla amplitude during noon is also consistent with the earlier CHAMP results and reflects inter-hemispheric field-aligned currents. These signatures relate to a statistical analysis for inter-hemispheric field-aligned currents and F-region dynamo currents conducted by Park et al. (2020) based on GRACE-FO data. GF2 observations are less clear for these low-latitude ionospheric signatures, a fact which is also supported by Park et al. (2020). On the night side, the GF1 residuals are very low which is expected due to the absence of strong ionospheric currents. However, an inconsistency is visible in GF2 B_C at the magnetic equator, as already noted in Fig. 3. This disturbance seems being artificial and is in opposite direction to the equatorial electrojet signatures on the dayside. Assuming that this artificial disturbance is not only confined to the night side, it might be the reason why the dayside equatorial GF2 B_C shows lower amplitudes than the expected 10 nT from the natural signal. Similar consideration seems true for all three components, which are in general more disturbed during nighttime at GF2 than at GF1 and appear artificial.

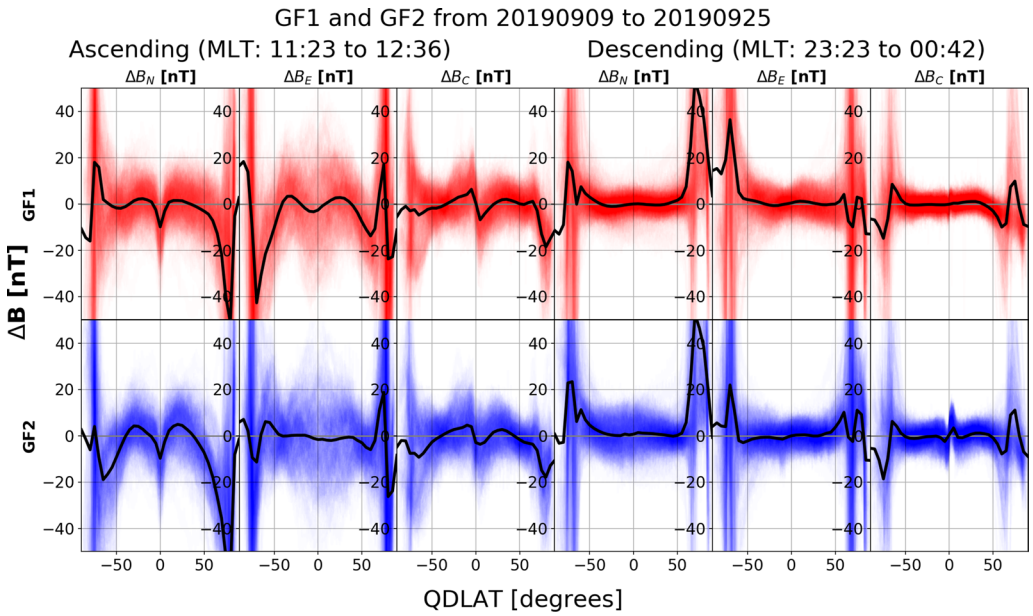

Fig. 4 Orbit-wise magnetic residual to CHAOS-7 (core, crustal and large-scale magnetospheric field) in NEC frame for September 2019 for ascending (12 MLT, left) and descending (00 MLT, right) orbits. The red lines correspond to GF1 and blue lines to GF2. Black lines provide mean values at each QDLAT

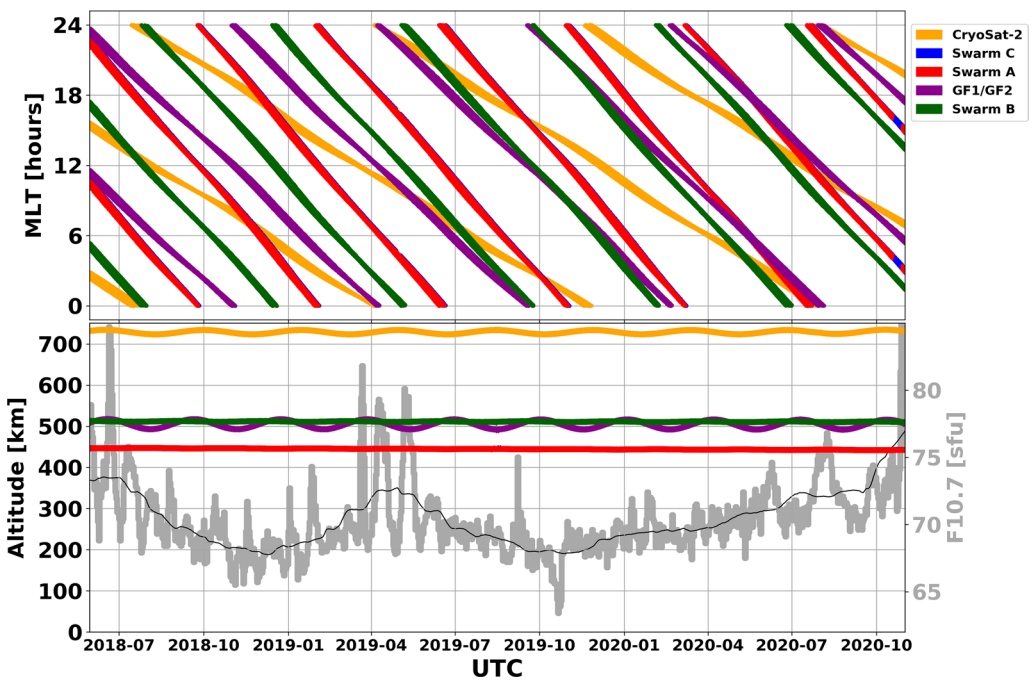

Fig. 5 Magnetic local times (top) and orbit altitude (bottom) at equator crossings of the GRACE-FO, Swarm, and CryoSat-2 missions, as well as the daily (grey) and monthly averaged (black) F10.7 index

Comparison to magnetic data of Swarm

Figure 5 shows the MLT and altitude evolution of the GRACE-FO, Swarm, and CryoSat-2 missions, as well as the daily (grey) and monthly averaged (black) solar flux index F10.7. GRACE-FO and Swarm B fly at similar altitudes and a conjunction in MLT between GRACE-FO and Swarm B occurred early November 2019. At this time, the solar flux index has been low with approximately $F10.7 = 70$ sfu ($1\,\text{sfu} = 10^{22}\,\text{W}\,\text{m}^{-2}\,\text{Hz}^{-1}$).

Figure 6 compares the magnetic data between the two missions during their conjunction interval between November 2 and November 14. Geomagnetic activity

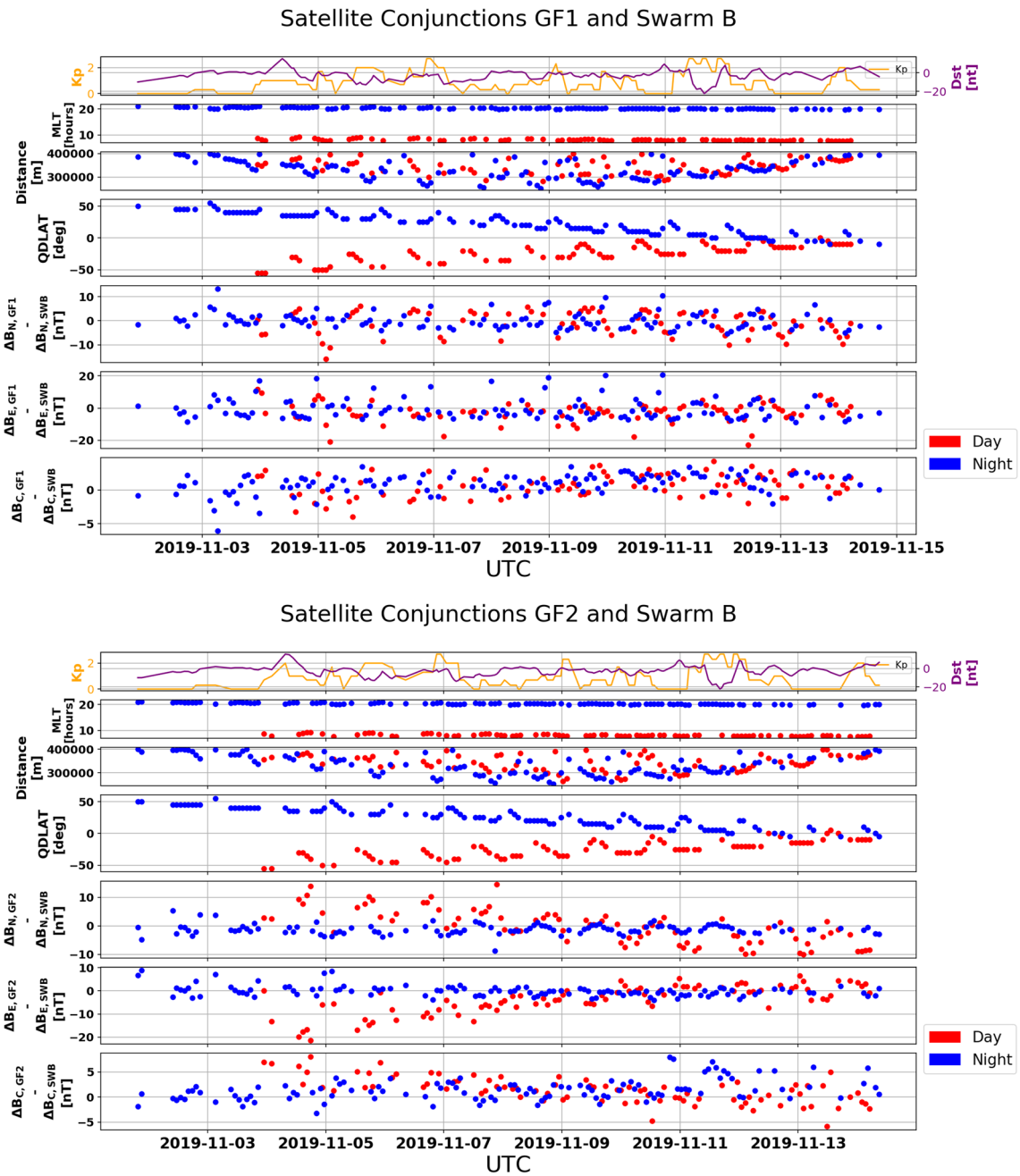

Fig. 6 GF1 (top) or GF2 (bottom) conjunctions with Swarm B. Panel 1: Kp and Dst indices, panel 2: magnetic local time of conjunction, panel 3: intra-satellite distance, panel 4: quasi-dipole latitude of conjunction, and panels 5–7: difference between magnetic residuals of GF1 or GF2 and Swarm B

was low with Kp $\leq 2^+$ and Dst ≥ -20 nT. The two missions were counter-rotating, e.g., the MLT at their respective equator crossings was ~10 MLT for the ascending node of GRACE-FO and for the descending node of Swarm B, and it was ~ 22 MLT for the descending/ascending nodes, respectively. We define a 'conjunction' when the distance between the GF1 or GF2 satellites and Swarm B were less than 400 km. Since the conjunctions occurred during counter-rotating orbital segments, they only lasted few seconds each. Panels 3 give the intra-satellite distance for each conjunction and panels 4 provide the mean QDLAT at which the conjunction happened. Panels 5–7 plot the differences between the residuals of the calibrated magnetic data to the respective CHAOS-7 predictions for GF1 or GF2 and Swarm B for each conjunction and for each magnetic component. The majority (>80%) of the differences of the single conjunctions are within ± 10 nT for all 3 components. The smallest scatter occurs for B_C, followed by that of B_N and then of B_E. This can have several reasons, such that different ionospheric currents affect different components at different latitudes. Another aspect is that $|B_C|$ includes the widest range of values with up to 65,000 nT, followed by $|B_N|$ up to 30,000 nT, and $|B_E|$ up to 15,000 nT. Variables with wider ranges can be estimated with lower uncertainty. The mean difference to Swarm B over all conjunctions is slightly larger for day time than for night time orbits, e.g., GF1 day time $\Delta(B_N, B_E, B_C) = (-1.02, -2.56, 0.73)$ nT, GF1 night time $\Delta(B_N, B_E, B_C) = (0.12, -0.41, 0.95)$ nT, GF2 day time $\Delta(B_N, B_E, B_C) = (-0.20, -3.72, 1.44)$ nT, and GF2 night time $\Delta(B_N, B_E, B_C) = (-1.18, -0.07, 1.47)$ nT. The less good agreement during day may result from dayside ionospheric currents which introduce stronger spatial and temporal variability of the magnetic field. The overall small differences between the GRACE-FO and the Swarm observations further support the high quality of the calibrated magnetic data set of the GRACE-FO mission.

The magnetic effect of the magnetospheric ring current during the August 26, 2018 storm

A geomagnetic storm with values of Dst < −150 nT occurred on August 26, 2018. During this time, all Swarm spacecraft, CryoSat-2, and GF1 were in orbit, and calibrated magnetic data are available for each of these missions. Unfortunately, GF2 does not provide magnetic data for August 2018. Figure 7 shows the evolution of the magnetic effects of the magnetospheric ring current, as well as the Dst index. The squares, triangles, and circles represent medians of residuals of the horizontal component of the magnetic field ($\sqrt{B_N^2 + B_E^2}$) within $\pm 20°$ QDLAT and projected to 0° QDLAT for each low-latitude orbital segment of the respective satellite. The residuals are with respect to the CHAOS-7 core and crustal field predictions. The large-scale magnetospheric field was not subtracted, and signatures from magnetospheric

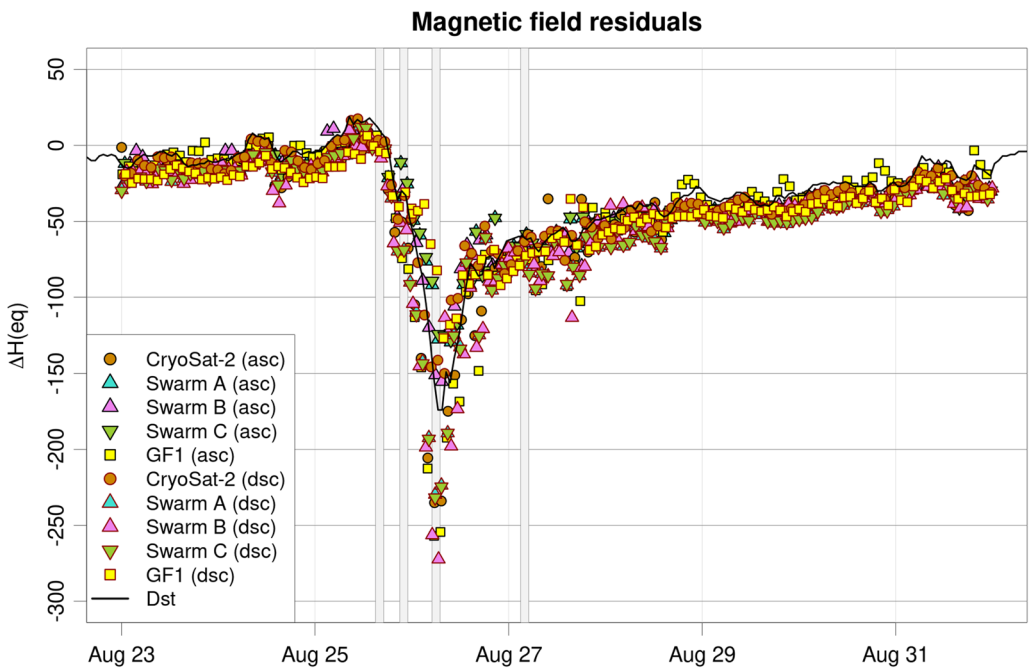

Fig. 7 Time-series of residuals of calibrated Swarm, CryoSat-2, and GF1 magnetic data to the core and crustal field of CHAOS-7 around the magnetic storm in August 2018. Ascending (asc) and descending (dsc) nodes are shown separately. The Dst index is also plotted. See text for details

currents (including its induced counterpart in Earth) remain included in the data. The point populations of all missions follow in generally well each other and the Dst index, despite the different retrieval technique for magnetospheric signatures in ground and satellite data. It is known from earlier studies that ground-based derived ring current signatures (such as for deriving the Dst index) show systematic differences to those derived in space (Maus and Lühr 2005; Olsen et al. 2005; Lühr et al. 2017), e.g., the ring current signal at LEO is generally more negative than at ground, which is also here reflected in an offset between the Dst index and the satellite-derived residuals. In addition, different groups of missions categorised in ascending and descending nodes appear to cluster and show an apparent offset to each other. This apparent offset between the categories represent local time differences of the magnetospheric ring current signature. Figure 8 shows the SuperMAG Magnetospheric Ring current indices (SMR, Newell and Gjerloev 2012) for the four local time sectors at midnight, dawn, noon, and dusk (00 MLT, 06 MLT, 12 MLT, and 18 MLT) together with the Dst index. Also here, a few differences between the two index groups may occur due to different retrieval techniques, such as in baseline determination or selection of observatories (e.g., Love and Gannon 2009; Gjerloev 2012; Newell and Gjerloev 2012). While the values for the four MLT sectors of the SMR are close to each other before the storm onset around 18 UTC on August 25, as well as during the recovery phase after about 18 UTC on August 27, they significantly deviate during the main phase of the storm, with highest values at 06 MLT and lowest at 18 MLT. The values at 12 MLT and 00 MLT are similar to each other and in-between the values at dawn and dusk.

Figure 9a–d shows four snapshots of magnetic residuals equatorward of $\pm 20°$ QDLAT and collected within 2 h time windows from each of the satellite missions, before the storm onset (16 UTC, August 25), shortly after the storm onset (23 UTC, August 25), during the main phase of the storm (06 UTC, August 26), and during the recovery phase (04 UTC, August 27). After the storm onset, a clear expansion of the magnetospheric field develops at the dusk side and the signal is least at dawn. This is in agreement with the SuperMAG indices, and the values are comparable with about -25 nT/-75 nT and -100 nT/-200 nT in panels b and c at dawn/dusk, respectively. The selected constellation of satellite missions did not cover midnight and noon, and less information is available from these MLT sectors. The described scenario is a typical storm behaviour and has been identified and discussed by statistical studies from LEO satellite observations or extended ground-based magnetic networks (e.g., Le et al. 2011; Pick et al. 2019). It has been attributed to either an asymmetric ring current component, to addition ionospheric currents, or to effects of

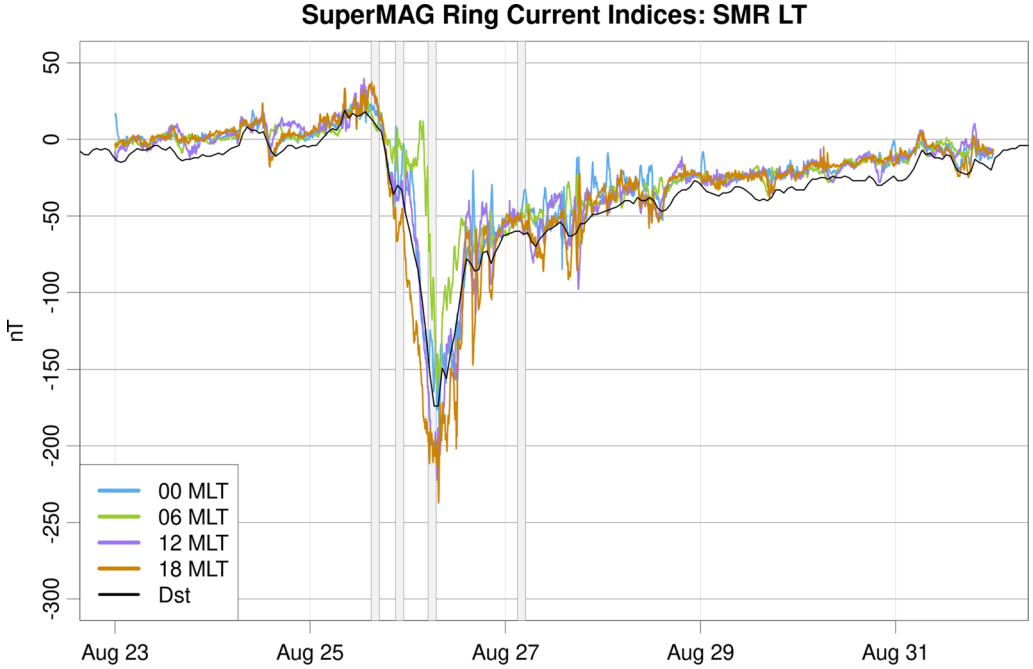

Fig. 8 SMR indices at 1 min resolution for local time sectors at 00 LT, 06 LT, 12 LT, and 18 LT. The Dst index is also plotted

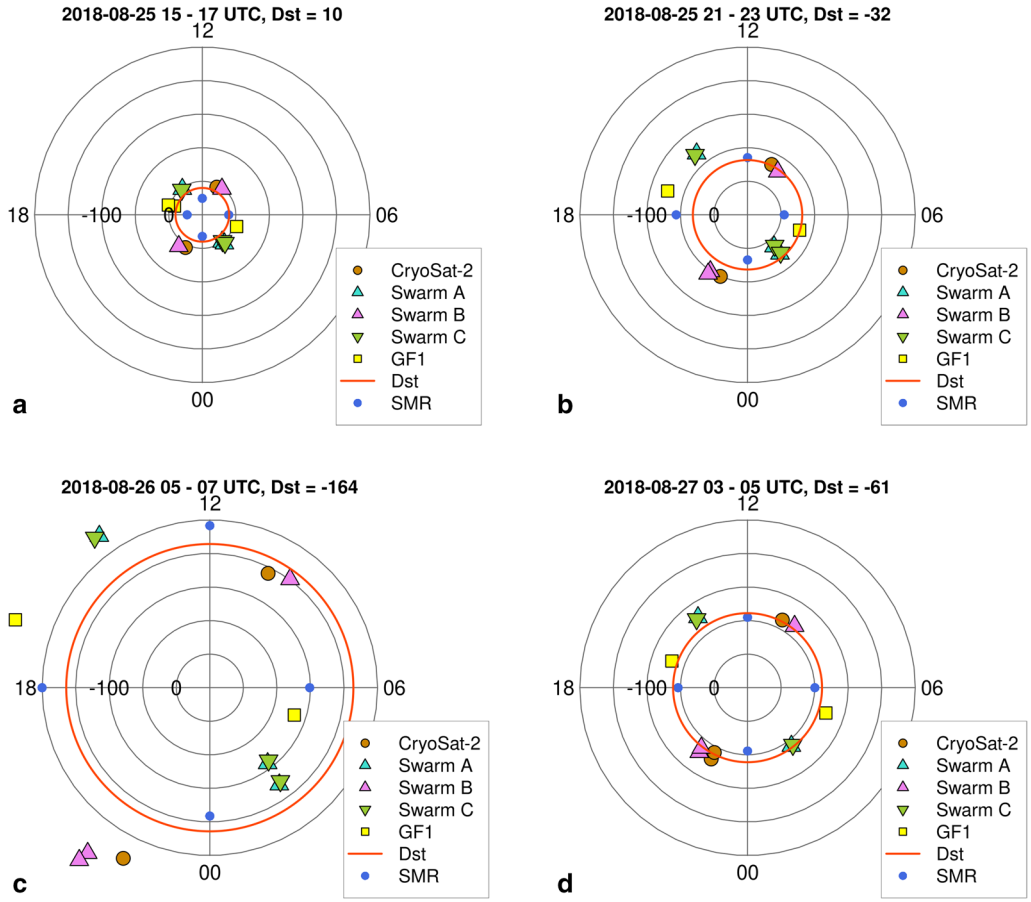

Fig. 9 MLT distribution of satellite magnetic field residuals, SMR, and Dst index for different UT. The integration time is 2 h and is provided in the title of each panel and indicated by vertical grey lines in Figs. 7 and 8. The black circles give reference to the magnitude of the satellite data and the indices

enhanced high-latitude R2 field-aligned currents during geomagnetic storms.

Auroral field-aligned currents

The calibrated magnetometer data from GF1 and GF2 were used to derive magnetic field-aligned currents. Therefore, we applied the processing algorithm, which is based on Ampères law and is similar to that used to derive Swarm single satellite field-aligned current (FAC) products available as the Swarm Level-2 product FACxTMS_2F (with $x = A, B, C$) from ESA and described in Ritter et al. (2013) and Kervalishvili (2017). We refer the reader to these documents for a detailed description of the algorithm. The method has also successfully been applied to magnetic observations from earlier missions, like CHAMP (e.g., Wang et al. 2005) and to DMSP (Xiong et al. 2020).

Figure 10 shows FACs derived from GF1 and GF2 data for an event on 31 October 2019 when they crossed the northern auroral latitudes. At this time, Kp $= 4^-$, AE ~ 100 nT (Auroral Electrojet index), and Dst ~ -7 nT. The event was chosen due to co-located data by Swarm B, which will be discussed in the next paragraph. The data of the two GRACE-FO satellites show similar FAC variations along their orbits, but with a time delay of about 24 s, the time difference when GF1 and GF2 reached the highest magnetic latitude of their orbits (upper panel).

The middle panel shows the time-series plotted along Apex latitude (MLAT, Richmond 1995; Emmert et al. 2010). FAC signatures derived from the two satellites compare well to each other in location of occurrence and in amplitude. Enhanced FAC events are observed between 65° and 72° and 70° and 83° MLAT on the dusk and dawn sides, respectively. At other latitudes, GRACE-FO FACs show a noise level less than 0.5 $\mu A/m^2$. After applying a low-pass filter with cut-off frequency of 20 s, the FAC profiles from the two satellites are nearly identical. This cut-off frequency ensures a cut-off for kinetic Alfvén waves that is observed to be at periods between

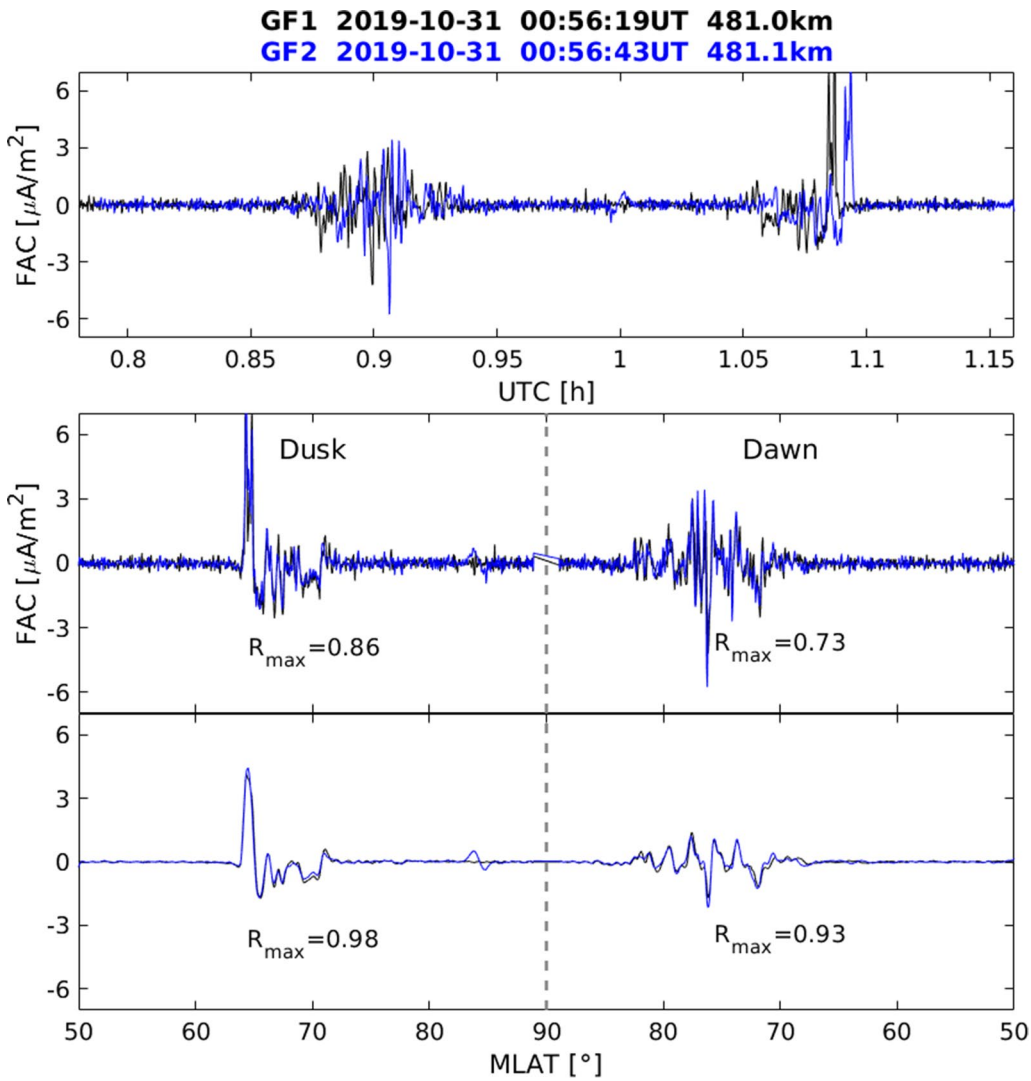

Fig. 10 FACs derived from GF1 and GF2 for an event at the Northern hemisphere on October 31, 2019. The data are shown in 1 s samplings (top, middle) and filtered by 20 s (bottom)

4 and 10 s depending on ionospheric conductivity (Ishii et al. 1992). The cross-correlation between the two time-series over MLAT maximises with $R_{\max} = 0.86/0.73$ for the 1 s-series and with $R_{\max} = 0.98/0.93$ when the 20 s filter was applied. This maximum correlation was found for zero time-shift for both the 1 s and 20 s-filtered FAC series. This result indicates that large-scale structures in the FAC event dominated and are persistent and almost stationary within 24 s, the time both satellites crossed the same area. This result is in agreement with Gjerloev et al. (2011) who applied magnetic data of the ST 5 constellation mission of 3 spacecraft following each other with varying separation between few seconds and 10 min. The mission was operational for 3 months within May and June 2006 and was launched in dawn–dusk orbit. They correlated the magnetic signatures of field-aligned currents of different scale sizes and concluded that FAC systems with scale sizes larger than 200 km (corresponding to 26 s for an average satellite velocity of 7.5 km/s) appear to be stable on time scales of about 1 min. When several years of GRACE-FO data will be available in future, similar studies can be conducted across all local times and seasons, with the only caveat of a fixed inter-spacecraft separation.

Figure 11 shows the same event, but comparing GF1 (black line) with Swarm B data (red line) during a conjunction event. GF1 and Swarm B were counter-rotating at similar magnetic local times (top panel),

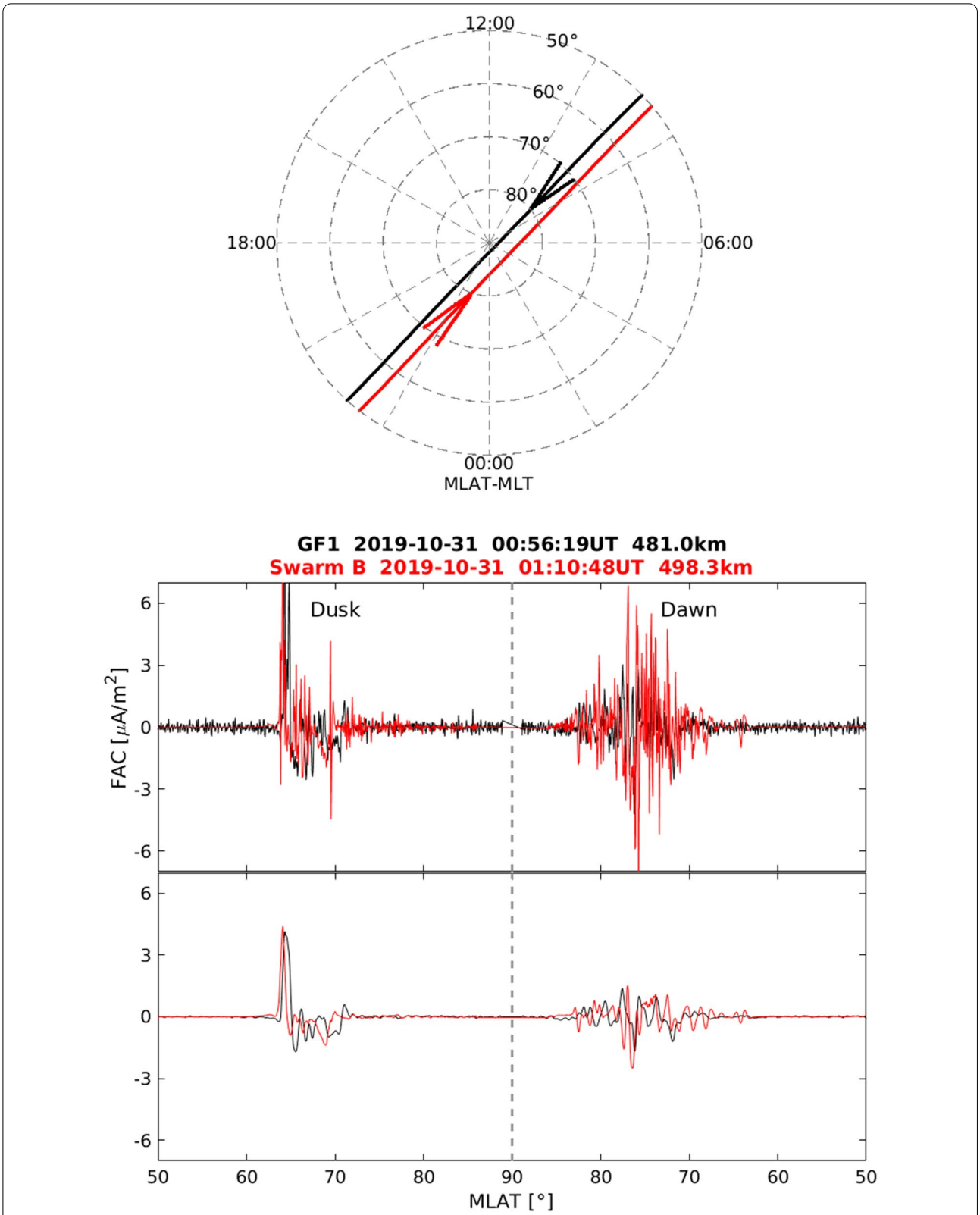

Fig. 11 Location of GF1 and Swarm B orbits as well as FACs derived from GF1 and Swarm B plotted over MLAT for the same event as in Fig. 10. The data are shown in 1 s samplings (middle) and filtered by 20 s (bottom)

and the UTC difference was about 14 min at the highest magnetic latitude of 88.8° and 85.8° of their respective orbits. Enhanced FAC signatures display at similar magnetic latitudes. The 1 Hz FAC time-series of Swarm B shows larger amplitudes than for GF1 at some locations (middle panel) which may hint to a possibly higher sensitivity of the Swarm science magnetometers, but may also represent differences in FAC structures at the slightly different locations and times. Away from the FAC event, Swarm shows a significantly lower noise level than GRACE-FO. After applying a low-pass filter with a cut-off frequency of 20 s to the 1 Hz data (lower panel) for both satellites, the large-scale structures show consistent features with similar amplitudes between the two missions. This example shows that large-scale FACs derived from GF1 and GF2 compare well with observations from high-precision magnetic data, e.g., from the Swarm mission, and thus can be considered reliable. However, due the enhanced noise level of nearly 0.5 $\mu A/m^2$, only case studies with event magnitudes well above this noise level can be investigated.

While the GRACE-FO magnetometers sample at a rate of 1 s without on-board filtering of higher sampled data, the Swarm 1 Hz observations are the result of a filtering based on 50 Hz samples. The comparison above shows that spot sampling at 1 Hz (such as for GRACE-FO) does not seem to significantly affect the results for FACs and especially is suitable to reliably derive signatures of FAC structures with scale lengths of 180 km or longer (corresponds to 24 s inter-spacecraft separation).

Figure 12 shows a statistical view of the MLAT versus MLT distributions of FACs derived from GF1. The data from the full data set available have been sorted into MLAT (1°) and MLT (1 h) for northward (IMF $B_z > 0$) and southward (IMF $B_z < 0$) interplanetary magnetic field (IMF) conditions, as well as separately for the two hemispheres. The FAC show clear Region 1 (R1) and Region 2 (R2) patterns, with higher intensity and expanding to lower latitudes for southward IMF B_z. For northward IMF B_z (NBZ), the known current pair NBZ appears poleward of the R1 sheet around local noon. The IMF B_z dependence of FAC derived from GF1 compares well to those of previous publications (e.g., Wang et al. 2008; Korth et al. 2010; Milan et al. 2017). Furthermore, the intensity of the FACs in the northern hemisphere is slightly higher than that in the southern hemisphere, which is consistent with the finding of Coxon et al. (2016) derived from AMPERE data, Laundal et al. (2018) and Workayehu et al. (2019) derived from Swarm observations, and with Xiong et al. (2020) derived from DMSP observations. These plots show that also small amplitudes near the noise level of GRACE-FO data are well accessible when they are applied in a statistical approach. This capability was also demonstrated by Park et al. (2020) who used CryoSat-2 and GRACE-FO data and successfully characterised interhemispheric field-aligned currents which have statistical amplitudes of as low as few nA/m^2.

Conclusions

The GRACE-FO mission carries vector magnetometers as part of its AOCS. After careful calibration and characterisation of artificial disturbances from the satellite, the magnetic data are applicable for scientific monitoring of the Earth's space environment. The mean residuals of the magnetic components to high-precision magnetic field models, such as CHAOS-7, are small with around a nanotesla for geomagnetic quiet periods and standard deviations are low with < 10 nT. These results are similar, e.g., to those of CryoSat-2 calibrated magnetometer data (Olsen et al. 2020). Strong support is provided by agreements between the magnetic residuals of the high-precision magnetic field Swarm mission within ± 10 nT during most of their conjunctions.

The calibrated GRACE-FO data can successfully be applied to case studies to high-amplitude events, such as signatures of the magnetospheric ring current of few tens to hundreds of nanotesla during geomagnetic storms. Especially in constellation with other LEO satellite missions flying at different orbits, this combination enables to describe the local time behaviour of the ring current signal. Auroral field-aligned currents are also reliably and well detectable, and those have signatures in the horizontal magnetic field components of several tens to hundreds of nanotesla. It was shown that for large-scale currents of scale lengths of 180 km or more compare well in amplitude with those derived from Swarm observations. Another opportunity is provided by the two-satellite constellation of GRACE-FO to investigate scale sizes of ionospheric structures. Only applied for a single auroral FAC event here, the soon multi-year mission will allow statistical approaches to characterise different local times and seasons. In addition, the constellation may be suitable to derive an enhanced algorithm to estimate large-scale FAC structures, where local stationarity of the FAC structures between the satellites is assumed, but

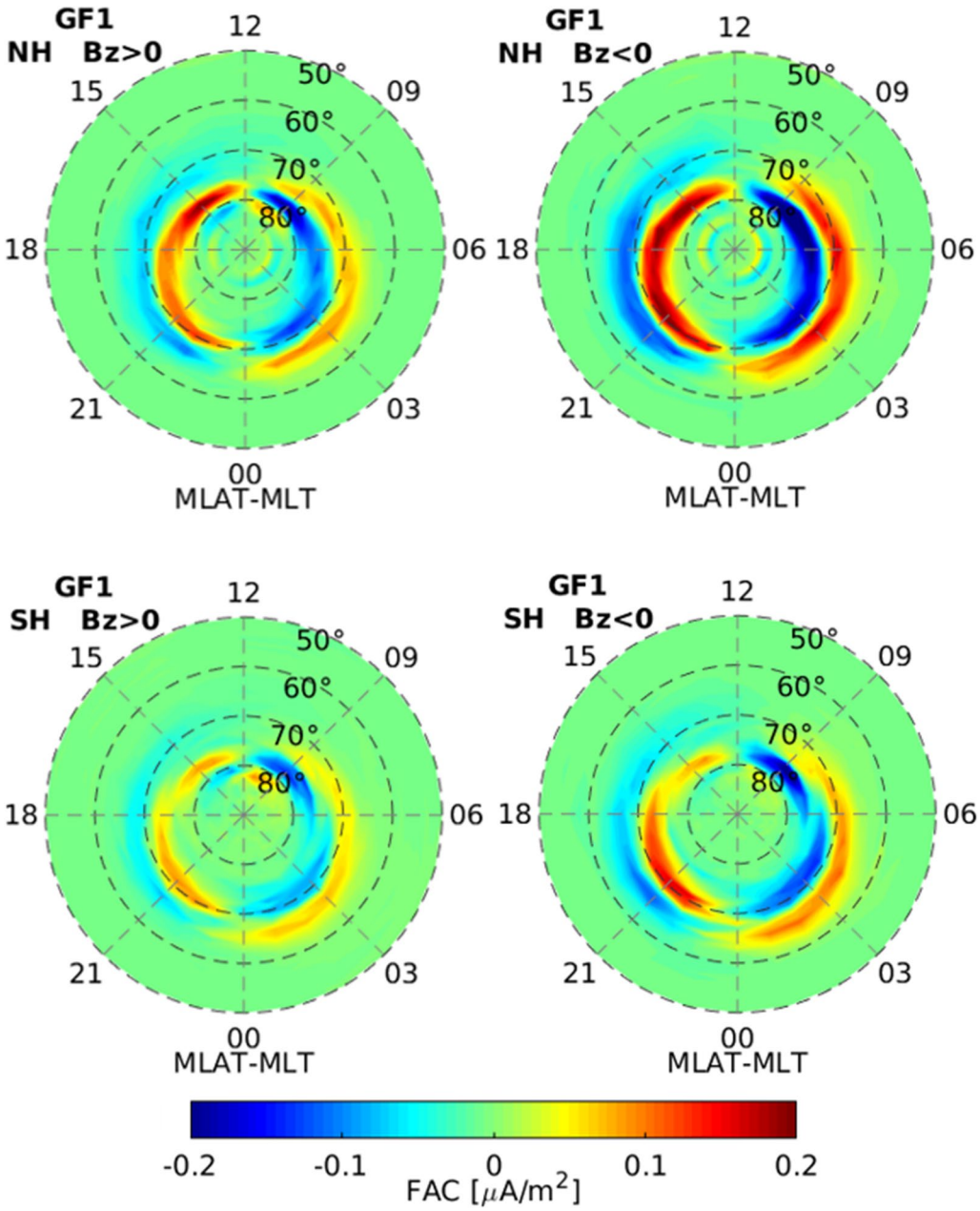

Fig. 12 MLAT vs MLT distribution of FACs derived from GF1 magnetic data for the Northern (top) and Southern (bottom) hemisphere and for IMF $B_z > 0$ (left) and IMF $B_z < 0$ (right)

the ambiguity resulting from temporal variations which is included in a single satellite approach can be dropped.

An exciting venue from the GRACE-FO constellation mission is its potential application of an improved characterisation of artificial spacecraft fields. The knowledge that the magnetometers on both spacecraft are identical, but flying with opposite direction through the ionosphere and magnetic field may further add in identifying suitable or improved characterisation parameters. Also, the GRACE-FO satellites can potentially be operated with both magnetometers (an active and a redundant one) switched on at each satellites. The mean of calibrated data of both instruments on one satellite is likely to further reduce the noise level.

Calibrated data from non-dedicated magnetometers in LEO have demonstrated high potential in extending the duration, the local time, and spatial distribution of available observations of Earth's space environment and

magnetic sources of the Earth's interior; especially, the combination with dedicated magnetic field missions and other missions carrying non-dedicated magnetometers, greatly enhance the scientific perspectives. Nevertheless, successful calibration relies on the availability of a high-precision magnetic field model that relies on high-precision data such as from the Swarm mission. Data from non-dedicated magnetometers at LEO can currently not replace the need for magnetic missions, but strongly enhance the monitoring of the geomagnetic field variability.

Abbreviations

AMPERE: Active Magnetometer and Planetary Electrodynamic Response Experiments; AOCS: Attitude and Orbit Control System; CASSIOPE: CAScade, Smallsat, and IOnospheric Polar Explorer; CHAMP: CHAllenging Minisatellite Payload; C/NOFS: Communications/Navigation Outage Forecasting System; CHAOS: CHAmp Ørsted SAC-C magnetic field model; CDF: Common Data Format; CSES: China Seismo-Electromagnetic Satellite; DMSP: Defense Meteorological Satellite Program; Dst: Geomagnetic Equatorial Disturbance Storm Time Index; ESA: European Space Agency; FAC: Field-Aligned Currents; FGM: Fluxgate Magnetometer; GFZ: Helmholtz Centre Potsdam, GFZ German Research Centre for Geosciences; GRACE-FO/GF: Gravity Recovery and Climate Experiment Follow-On; HK: Housekeeping; ICRF: International Celestial Reference Frame; IGRF: International Geomagnetic Reference Field IGRF-13; ISDC: Information System and Data Center at GFZ; ITRF: International Terrestrial Reference Frame; JPL: Jet Propulsion Laboratory; Kp: Geomagnetic index (Planetare Kennziffer); L1b: GRACE-FO Level 1b data; LEO: Low Earth Orbit; MLAT: Modified Apex Latitude; MLT: Magnetic Local Time; MTQ: Magnetorquer; NASA: National Aeronautics and Space Administration; NBZ: Northward B_z ; NEC: North, East, Center coordinate system; QDLAT: Quasi-dipole latitude; SAC-C: Satellite de Aplicaciones Cientifico-B; SRF: Science Reference Frame; STR: Star cameras (Star TRackers).

Acknowledgements

We thank Jaeheung Park and Alexander Grayver for fruitful discussions. We acknowledge Krzysztof Snopek for GRACE-FO mission operations and Christoph Dahle for assistance at ISDC. GRACE-FO is operated under a partnership between NASA and the Helmholtz Centre Potsdam, GFZ, German Research Centre for Geosciences. The European Space Agency (ESA) is gratefully acknowledged for providing the Swarm data. Kp is provided by GFZ, the Dst and AE indices by the Geomagnetic World Data Centre Kyoto, and F10.7 by the Dominion Radio Astrophysical Observatory and Natural Resources Canada.

Authors' contributions

CS defined the study. IM pre-processed and calibrated the data. TU provided data and advised on satellite operations. JR derived FACs. CS, CX, IM, MR, and KSR analysed the data. CS, CX, and YY interpreted the results. CS, IM, and CX wrote the manuscript. All authors read and approved the final manuscript.

Funding

Open Access funding enabled and organized by Projekt DEAL. This study has been partly supported by Swarm DISC activities funded by ESA under contract no. 4000109587/13/I-NB. KSR is supported through HEIBRIDS—Helmholtz Einstein International Berlin Research School in Data Science under contract no. HIDSS-0001.

Availability of data and materials

The data generated and analysed in this paper are available at ftp://isdcftp.gfz-potsdam.de/grace-fo/MAGNETIC_FIELD (Michaelis et al. 2021).

Competing interests

The authors declare that they have no competing interests.

Author details

[1] Helmholtz Centre Potsdam, GFZ German Research Centre for Geosciences, Telegrafenberg, 14473 Potsdam, Germany. [2] Faculty of Science, University of Potsdam, Karl-Liebknecht-Str. 24-25, 14476 Potsdam, Germany. [3] Airbus Defence and Space GmbH, Claude-Dornier-Straße, 88090 Immenstaad am Bodensee, Germany. [4] Electrical Engineering and Computer Science, Technical University of Berlin, Ernst-Reuter-Platz 7, 10587 Berlin, Germany.

Received: 15 September 2020 Accepted: 18 January 2021
Published online: 15 February 2021

References

Alken P (2016) Observations and modeling of the ionospheric gravity and diamagnetic current systems from CHAMP and Swarm measurements. J Geophys Res 121(1):589–601. https://doi.org/10.1002/2015JA022163

Alken P, Maus S, Lühr H, Redmon RJ, Rich F, Bowman B, O'Malley SM (2014) Geomagnetic main field modeling with DMSP. J Geophys Res 119(5):4010–4025. https://doi.org/10.1002/2013JA019754

Alken P, Olsen N, Finlay C (2020a) Co-estimation of geomagnetic field and in-orbit fluxgate magnetometer calibration parameters. Earth Planets Space 72:49. https://doi.org/10.1186/s40623-020-01163-9

Alken P, Thébault E, Beggan C, Amit H, Aubert J, Baerenzung J, Bondar TN, Brown W, Califf S, Chambodut A, Chulliat A, Cox G, Finlay CC, Fournier A, Gillet N, Grayver A, Hammer M, Holschneider M, Huder L, Hulot G, Jager T, Kloss C, Korte M, Kuang W, Kuvshinov A, Langlais B, Léger JM, Lesur V, Livermore PW, Jones FJ, Macmillan S, Magnes W, Mandea M, Marsal S, Matzka J, Metman MC, Minami T, Morschhauser A, Mound JE, Nair M, Nakano S, Olsen N, Pavón-Carrasco FJ, Petrov VG, Ropp G, Rother M, Sabaka TJ, Sanchez S, Saturnino D, Schnepf N, Shen X, Stolle C, Tangborn A, Tøffner-Clausen L, Toh H, Torta JM, Varner J, Vigneron P, Vervelidou F, Wardinski I, Wicht J, Woods A, Yang Y, Zeren Z, Zhour B (2020b) International geomagnetic reference field: the thirteenth generation. Earth Planets Space. https://doi.org/10.1186/s40623-020-01288-x

Anderson B, Takahashi K, Toth B (2000) Sensing global Birkeland currents with Iridium engineering magnetometer data. Geophys Res Lett 27:4045–4048. https://doi.org/10.1029/2000GL000094

Billingsley (2020) Billingsley TFM100SH magnetometer. https://magnetometer.com/products/fluxgate-magnetometers/tfm100s, https://magnetometer.com/wp-content/uploads/magnetometer-comaparison.pdf, https://magnetometer.com/wp-content/uploads/TFM100S-Spec-Sheet-February-2008.pdf

Brauer P, Merayo JMG, Nielsen OV, Primdahl F, Petersen JR (1997) Transverse field effect in fluxgate sensors. Sens Actuators A Phys 59:70–74. https://doi.org/10.1016/s0924-4247(97)01416-7

Carter JA, Milan SE, Coxon JC, Walach MT, Anderson BJ (2016) Average field-aligned current configuration parameterized by solar wind conditions. J Geophys Res 121:1294–1307. https://doi.org/10.1002/2015JA021567

Coxon JC, Milan SE, Carter JA, Clausen LBN, Anderson BJ, Korth H (2016) Seasonal and diurnal variations in AMPERE observations of the Birkeland currents compared to modeled results. J Geophys Res 121:1294–1307. https://doi.org/10.1002/2015JA022050

Emmert JT, Richmond AD, Drob DP (2010) A computationally compact representation of magnetic apex and quasi-dipole coordinates with smooth base vectors. J Geophys Res 115:A08322. https://doi.org/10.1029/2010JA015326

Finlay CC, Kloss C, Olsen N, Hammer M, Tøffner-Clausen L (2019) DTU candidate models for IGRF-13. Technical report, DTU Space, National Space Institute. http://www.spacecenter.dk/files/magnetic-models/CHAOS-7/

Finlay CC, Kloss C, Olsen N, Hammer MD, Tøffner-Clausen L, Grayver A, Kuvshinov A (2020) The CHAOS-7 geomagnetic field model and observed changes in the South Atlantic anomaly. Earth Planets Space. https://doi.org/10.1186/s40623-020-01252-9

Gjerloev JW (2012) The SuperMag data processing technique. J Geophys Res Space Phys. https://doi.org/10.1029/2012JA017683

Gjerloev JW, Ohtani S, Iijima T, Anderson B, Slavin J, Le G (2011) Characteristics of the terrestrial field-aligned current system. Ann Geophys 29:1713–1729. https://doi.org/10.5194/angeo-29-1713-2011

Grayver AV, Schnepf NR, Kuvshinov AV, Sabaka TJ, Manoj C, Olsen N (2016) Satellite tidal magnetic signals constrain oceanic lithosphere-asthenosphere boundary. Sci Adv 2(9):e1600798. https://doi.org/10.1126/sciadv.1600798

Hulot G, Eymin C, Langlais B, Mandea M, Olsen N (2002) Small-scale structure of the geodynamo inferred from Ørsted and Magsat satellite data. Nature 416:620–623. https://doi.org/10.1038/416620a

IAU SOFA Board (2019) IAU SOFA software collection. http://www.iausofa.org

IERS (2020) International Earth rotation and reference systems service (IERS) Earth Orientation Center, Bulletin B. ftp://hpiers.obspm.fr/eop-pc/bul/bulb_new

Ishii M, Sugiura M, Iyemori T, Slavin JA (1992) Correlation between magnetic and electric field perturbations in the field-aligned current regions deduced from de 2 observations. J Geophys Res Space Phys 97(A9):13877–13887. https://doi.org/10.1029/92JA00110

Kervalishvili G, et al (2017) Swarm L2 TEC product description, SW-TR-GFZ-GS-0007, rev. 4. Technical report, European Space Agency (ESA). https://earth.esa.int/documents/10174/1514862/Swarm_Level-2_TEC_Product_Description

Knipp D, Eriksson S, Kilcommons L, Crowley G, Lei J, Hairston M, Drake K (2011) Extreme Poynting flux in the dayside thermosphere: examples and statistics. Geophys Res Lett. https://doi.org/10.1029/2011GL048302

Korth H, Anderson B, Waters C (2010) Statistical analysis of the dependence of large-scale Birkeland currents on solar wind parameters. Ann Geophys 28:515–530. https://doi.org/10.5194/angeo-28-515-2010

Landerer FW, Flechtner FM, Save H, Webb FH, Bandikova T, Bertiger WI, Bettadpur SV, Byun SH, Dahle C, Dobslaw H, Fahnestock E, Harvey N, Kang Z, Kruizinga GLH, Loomis BD, McCullough C, Murböck M, Nagel P, Paik M, Pie N, Poole S, Strekalov D, Tamisiea ME, Wang F, Watkins MM, Wen HY, Wiese DN, Yuan DN (2020) Extending the global mass change data record: GRACE follow-on instrument and science data performance. Geophys Res Lett 47(12):e2020GL088306. https://doi.org/10.1029/2020GL088306

Laundal KM, Finlay CC, Olsen N, Reistad JP (2018) Solar wind and seasonal influence on ionospheric currents from Swarm and CHAMP measurements. J Geophys Res 123:4402–4429. https://doi.org/10.1029/2018JA025387

Laundal KM, Hatch SM, Moretto T (2019) Magnetic effects of plasma pressure gradients in the upper F region. Geophys Res Lett 46(5):2355–2363. https://doi.org/10.1029/2019GL081980

Le G, Burke W, Pfaff R, Freudenreich H, Maus S, Lühr H (2011) C/NOFS measurements of magnetic perturbations in the low-latitude ionosphere during magnetic storms. J Geophys Res 116:A12230. https://doi.org/10.1029/2011JA017026

Livermore P, Hollerbach R, Finlay C (2017) An accelerating high-latitude jet in Earth's core. Nat Geosci 10:62–68. https://doi.org/10.1038/ngeo2859

Love JJ, Gannon JL (2009) Revised D_{st} and the epicycles of magnetic disturbance: 1958–2007. Ann Geophys 27(8):3101–3131. https://doi.org/10.5194/angeo-27-3101-2009

Lühr H, Maus S (2006) Direct observation of the F region dynamo currents and the spatial structure of the EEJ by CHAMP. Geophys Res Lett. https://doi.org/10.1029/2006GL028374

Lühr H, Xiong C, Olsen N, Le G (2017) Near-Earth magnetic field effects of large-scale magnetospheric currents. Space Sci Rev 206:521–545. https://doi.org/10.1007/s11214-016-0267-y

Maus S, Lühr H (2005) Signature of the quiet-time magnetospheric magnetic field and its electromagnetic induction in the rotating Earth. Geophys J Int 162:755–763. https://doi.org/10.1111/j.1365-246X.2005.02691.x

Maus S, Lühr H, Rother M, Hemant K, Balasis G, Ritter P, Stolle C (2007) Fifth-generation lithospheric magnetic field model from CHAMP satellite measurements. Geochem Geophys Geosyst. https://doi.org/10.1029/2006GC001521

McGranaghan RM, Mannucci AJ, Forsyth C (2017) A comprehensive analysis of multiscale field-aligned currents: characteristics, controlling parameters, and relationships. J Geophys Res 122(12):11931–11960. https://doi.org/10.1002/2017JA024742

Michaelis I, Stolle C, Rother M (2021) GRACE-FO calibrated and characterized magnetometer data. V. 0201. GFZ Data Services. https://doi.org/10.5880/GFZ.2.3.2021.002

Milan SE, Clausen LBN, Coxon JC et al (2017) Overview of solar wind-magnetosphere-ionosphere-atmosphere coupling and the generation of magnetospheric currents. Space Sci Rev 206:547–573. https://doi.org/10.1007/s11214-017-0333-0

Miles DM, Mann IR, Pakhotin IP, Burchill JK, Howarth AD, Knudsen DJ, Lysak RL, Wallis DD, Cogger LL, Yau AW (2018) Alfvénic dynamics and fine structuring of discrete auroral arcs: Swarm and e-POP observations. Geophys Res Lett 45:545–555. https://doi.org/10.1002/2017GL076051

Newell PT, Gjerloev JW (2012) SuperMAG-based partial ring current indices. J Geophys Res 117:A05215. https://doi.org/10.1029/2012JA017586

Olsen N (1997) Ionospheric F region currents at middle and low latitudes estimated from Magsat data. J Geophys Res 102(A3):4563–4576. https://doi.org/10.1029/96JA02949

Olsen N, Stolle C (2012) Satellite geomagnetism. Annu Rev Earth and Planet Sci 40(1):441–465. https://doi.org/10.1146/annurev-earth-042711-105540

Olsen N, Sabaka T, Lowes F (2005) New parameterization of external and induced fields in geomagnetic field modeling, and a candidate model for IGRF 2005. Earth Planets Space 57(12):1141–1149. https://doi.org/10.1186/BF03351897

Olsen N, Ravat D, Finlay CC, Kother LK (2017) LCS-1: a high-resolution global model of the lithospheric magnetic field derived from CHAMP and Swarm satellite observations. Geophys J Int 211(3):1461–1477. https://doi.org/10.1093/gji/ggx381

Olsen N, Albini G, Bouffard J, Parrinello T, Tøffner-Clausen L (2020) Magnetic observations from CryoSat-2: calibration and processing of satellite platform magnetometer data. Earth Planets Space 72:48. https://doi.org/10.1186/s40623-020-01171-9

Park J, Lühr H, Min KW (2010) Characteristics of F-region dynamo currents deduced from CHAMP magnetic field measurements. J Geophys Res. https://doi.org/10.1029/2010JA015604

Park J, Stolle C, Yamazaki Y, Rauberg J, Michaelis I, Olsen N (2020) Diagnosing low-/mid-latitude ionospheric currents using platform magnetometers: CryoSat-2 and GRACE-FO. Earth Planets Space 72:162. https://doi.org/10.1186/s40623-020-01274-3

Pick L, Effenberger F, Zhelavskaya I, Korte M (2019) A statistical classifier for historical geomagnetic storm drivers derived solely from ground-based magnetic field measurements. Earth Space Science 6:2000–2015. https://doi.org/10.1029/2019EA000726

Richmond A (1995) Ionospheric electrodynamics using magnetic apex coordinates. J Geomagn Geoelectr 47:191–212. https://doi.org/10.5636/jgg.47.191

Ritter P, Lühr H, Rauberg J (2013) Determining field-aligned currents with the Swarm constellation mission. Earth Planets Space 65:1285–1294. https://doi.org/10.5047/eps.2013.09.006

Rodríguez-Zuluaga J, Stolle C (2019) Interhemispheric field-aligned currents at the edges of equatorial plasma depletions. Sci Rep 9(1233):1–8. https://doi.org/10.1038/s41598-018-37955-z

Seeber G (2003) Satellite Geodesy, 2nd edn. Walter de Gruyter, Berlin. https://doi.org/10.1515/9783110200089

Stolle C, Lühr H, Rother M, Balasis G (2006) Magnetic signatures of equatorial spread F, as observed by the CHAMP satellite. J Geophys Res 111:A02304. https://doi.org/10.1029/2005JA011184

Tapley BD, Bettadpur S, Watkins M, Reigber C (2004) The gravity recovery and climate experiment: mission overview and early results. Geophys Res Lett 31:L09607. https://doi.org/10.1029/2004GL019920

Wang H, Lühr H, Ma SY (2005) Solar zenith angle and merging electric field control of field-aligned currents: a statistical study of the Southern Hemisphere. J Geophys Res 110:A03306. https://doi.org/10.1029/2004JA010530

Wang H, Ridley AJ, Lühr H (2008) SWMF simulation of field-aligned currents for a varying northward and duskward IMF with nonzero dipole tilt. Ann Geophys 26:1461–1477. https://doi.org/10.5194/angeo-26-1461-2008

Wertz JR (1978) Spacecraft attitude determination and control, vol 73. Springer, Amsterdam. https://doi.org/10.1007/978-94-009-9907-7

Workayehu AB, Vanhamäki H, Aikio AT (2019) Field-aligned and horizontal currents in the Northern and Southern Hemispheres from the Swarm satellite. J Geophys Res 124:7231–7246. https://doi.org/10.1029/2019JA026835

Xiong C, Stolle C, Alken P, Rauberg J (2020) Relationship between large-scale ionospheric field-aligned currents and electron/ion precipitations: DMSP observations. Earth Planets Space 72:147. https://doi.org/10.1186/s40623-020-01286-z

Yang Y, Hulot G, Vigneron P, Shen X, Zeren Z, Zhou B, Magnes W, Olsen N, Tøffner-Clausen L, Huang J, Zhang X, Yuan S, Wang L, Cheng B, Pollinger A, Lammegger R, Dai J, Lin J, Guo F, Yu J, Wang J, Wu Y, Zhao X, Zhu X

(2020) The CSES global geomagnetic field model (CGGM): an IGRF type global geomagnetic field model based on data from the China Seismo-Electromagnetic Satellite. Earth Planets Space. https://doi.org/10.1186/s40623-020-01316-w

Publisher's Note